Chapter 5

Physical Properties of the Ionized Gas from the Low Resolution Survey

The intensity of recombination lines at different frequencies is determined by the physical properties of the ionized gas emitting the lines and the intensity of the background radiation field. The physical properties of interest are the electron temperature, the electron density and the physical size of the region. In this chapter we shall try to estimate or place constraints on the physical properties of the ionized gas responsible for the RRL emission observed in the low resolution survey. A brief discussion of the relevant equations used for modeling the RRL emission is presented. The theory of RRLs in the context of low frequency observations has been discussed in detail by Shaver (1975). We present here the details of a simple model used for the interpretation of the data and a discussion on the sensitivity of low frequency RRL observations to the physical properties of the ionized gas. The physical properties of the ionized gas towards positions where RRL data is available at 327 MHz and 1.4 GHz are derived using the simple model. The derived parameters are then used to compute the C II 158 μm and N II 205 μm line intensities and the free-free absorption of the galactic non-thermal emission near 34.5 MHz due to this gas. The estimated values are then compared with the observed values available in the literature.

5.1 Some Theory of RRL

In an RRL observation the parameters measured are the center frequency, the line width, the line intensity and the continuum intensity near the observed frequency. These parameters along with some additional information are used to deduce the properties of the line emitting region.

5.1.1 Line Frequency and Line Width

The rest frequency of a recombination line is given by the Rydberg relation

$$\nu = R_A c Z^2 \left(\frac{1}{n^2} - \frac{1}{(n+\Delta n)^2} \right) , \tag{5.1}$$

where $R_A = R_\infty(1 + \frac{m_e}{M_A})^{-1}$, R_∞ is the Rydberg constant, m_e and M_A are the electron and atomic masses respectively, c is the velocity of light, Z is the atomic number, n is the principal quantum number and Δn is the difference in the quantum numbers of the energy states. For hydrogen the value of R_A is 109,677.6 cm^{-1} , for helium it is 109,772.3 cm^{-1} and for carbon it is 109,732.3 cm^{-1}. The difference between the measured center frequency and the rest frequency is usually attributed to bulk motion of the cloud relative to a standard reference frame. For galactic observations, the Local Standard of Rest (LSR) is commonly used as the frame of reference. Note that in Equation 5.1 the presence of the atomic mass (M_A) produces a relative shift in the rest frequencies of line emission of different species of hydrogenic atoms.

The main physical processes that affect the width of the line are Doppler and pressure broadening. The profile function represents the probability of photon emission at frequencies about the center frequency. The profile function due to Doppler broadening is a Gaussian with a FWHM (full width at half maximum) given by

$$\Delta V_{LD} = \sqrt{0.0462\frac{T_e}{M_A} + \frac{2}{3} < V_t^2 >} \quad \text{km s}^{-1}, \tag{5.2}$$

where T_e is the electron temperature in K of the ionized gas, M_A is the mass of the atom in a.m.u and $< V_t^2 >^{1/2}$ is the R.M.S velocity in km s^{-1} due to turbulence. For the case of pressure broadening, the profile function is a Lorentzian with a width

$$\Delta V_{LP} = 1.7 \times 10^{-13}\frac{n_e n^{7.4}}{T_e^{0.1}}(1 + \frac{m_e}{M_A}) \qquad \text{km s}^{-1}\ . \tag{5.3}$$

Equation 5.3 is valid for the temperature range $\frac{1.6\times10^5}{n} \leq T_e \leq 1.6 \times 10^5$ where n is the principal quantum number, n_e (cm^{-3}) is the electron density, T_e (K) is the temperature.

In general, the profile function is a convolution of the two profiles, a Gaussian and a Lorentzian, which results in a Voigt profile. An approximate relation for the net FWHM is

$$\Delta V^2 = \Delta V_{LD}^2 + \Delta V_{LP}^2. \tag{5.4}$$

5.1.2 Continuum and Line Optical Depths

For computing the line intensity, a knowledge of line and continuum optical depths are required. The optical depth depends on the physical processes producing the radiation. In the case of continuum emission from a thermal plasma, the physical process is thermal bremsstrahlung and its optical depth is approximately (Altenhoff et al. 1960)

$$\tau_{C\nu} \approx 8.235 \times 10^{-2}\ EM\ T_e^{-1.35}\nu^{-2.1}, \tag{5.5}$$

where $EM = \int_0^L n_e^2 dl$ is the emission measure in pc cm^{-6}, L is the line of sight extent of the ionized gas, T_e is in K and ν is in GHz. The expression is valid for $\nu \ll 10^{10}T_e$ and $T_e < 9 \times 10^5$ K.

The line optical depth depends on the level populations. In the thermal plasma of interest, usually the velocity distribution of all particles are close to Maxwellian and hence a unique kinetic temperature (T_e) can be defined. The level population are therefore conveniently expressed in terms of the kinetic temperature. If the excitation temperature of the energy levels of interest is equal to the kinetic temperature, the

situation is called Local Thermodynamic Equilibrium (LTE) else non-LTE. In astrophysical plasma of interest, normally non-LTE situation prevails. In such a case, the strategy is to compute the line optical depth in terms of the LTE optical depth and a deviation from it is represented by the departure coefficients b_n and β_n. The departure coefficients are defined by the equations

$$b_n \equiv \frac{N_n}{N_n^*}, \tag{5.6}$$

$$\beta_n \equiv \frac{\left(1 - \frac{b_m}{b_n}\, e^{-E_{nm}/kT_e}\right)}{\left(1 - e^{-E_{nm}/kT_e}\right)} \approx \left(1 - \frac{d(ln(b_n))}{dn}\Delta n \frac{kT_e}{h\nu}\right). \tag{5.7}$$

Here b_n and b_m are the departure coefficients for state n and m respectively, N_n^* and N_n represents the atomic level population of the state n in LTE and non-LTE respectively, E_{nm} is the energy difference between states m and n and $\Delta n = n - m$. The expression for the non-LTE line optical depth for $\Delta n = 1$ transition in hydrogenic atoms is given by

$$\tau_{L\nu} = b_n \beta_n \tau_{L\nu}^* = b_n \beta_n\, 9.7 \times 10^7 \frac{EM\, n^3}{R_A\, T_e^{5/2}\, \Delta V_{LD}} \frac{e^{1.58\times10^5/n^2 T_e}}{(1 + 1.48\frac{\Delta V_{LP}}{\Delta V_{LD}})}, \tag{5.8}$$

where EM is in pc cm^{-6}, T_e is in K, ΔV_{LD} is in km s^{-1} and R_A is the Rydberg constant in cm^{-1}. $\tau_{L\nu}^*$ is the LTE optical depth.

The computation of the departure coefficients is described in the next section. The value of the departure coefficients depends on various factors such as the electron density, temperature and background radiation field (see below). The computed values of b_n are typically close to unity. However β_n can attain large negative values (see Roelfsema & Goss 1992), which make the optical depth negative (see Equation 5.8). Thus the coefficient β_n plays a significant role in the stimulated emission of RRLs at low frequencies.

5.1.3 Computation of the Departure coefficients

The departure coefficients are calculated by assuming a statistical equilibrium for the level population. An equilibrium is established when the time derivative of the level population is zero. This happens when the total rate of population due to various physical processes and total rate of depopulation are equal. An equation stating this equilibrium condition can be written in terms of the b_n coefficients for each and every energy level. The various processes considered are spontaneous and stimulated emission, absorption, collisional excitation and de-excitation, collisional and radiative ionization and recombination. For atoms with more than one electron, dielectronic-like recombination is also considered. The departure coefficients and their derivatives are computed iteratively for each energy state.

For the work presented in this thesis, we have used the computer code originally developed by Brocklehurst & Salem (1977) and later modified by Walmsley & Watson (1982) and Payne, Anantharamaiah & Erickson (1994) for the computation of b_n and

β_n coefficients. The non-thermal background temperature at 100 MHz, T_{R100}, and its spectral index α are input parameters. We used $T_{R100} = 10{,}000$ K and $\alpha = -2.7$ and the computation is performed assuming a pure hydrogenic case.

5.2 A Simple Model

One of the aims of any observations of RRL is to estimate the physical properties of the line emitting region, such as the electron density, temperature and size. The observed parameters that are used for the estimation are the line antenna temperature, the line width and the continuum antenna temperature from the same direction. In the case of galactic RRL observations, the LSR velocity of the line is used to obtain information about the distance to the source assuming a galactic rotation model. In this section we describe a physical model which is used to estimate the properties of the ionized gas responsible for line emission from the observed line parameters.

We consider a single homogeneous ionized cloud embedded in the galactic non-thermal background radiation field. Let the line of sight extent of the cloud be L_{cloud} and it is at a distance of D_{cloud} from the observer. The observed galactic background radiation intensity, which is mostly due to synchrotron emission from relativistic plasma, be $I_{\nu bg}$. The line intensity can be obtained by solving the radiative transfer equation. The source function S_ν in this case has contribution from two sources – (1) radiation generated in the cloud and (2) radiation generated due to the background at the cloud position. The source function can be written as

$$S_\nu = \frac{j_{\nu cloud} + \tilde{j}_{\nu bg}}{\kappa_\nu + \kappa_{\nu bg}} \approx S_{\nu cloud} + \frac{\tilde{j}_{\nu bg}}{\kappa_\nu} , \tag{5.9}$$

where we have assumed $\kappa_\nu \gg \kappa_{\nu bg}$. κ_ν and $\kappa_{\nu bg}$ are the absorption coefficient of the cloud and the relativistic plasma respectively, $j_{\nu cloud}$ is the emission coefficient of the cloud, $\tilde{j}_{\nu bg}$ is the mean value of the emission coefficient of the relativistic plasma and $S_{\nu cloud}$ is the source function of the cloud. Using the formal solution of radiative transfer equation, we get

$$I_\nu = I_{0bg,\nu} e^{-\tau_\nu} + \left(S_{\nu cloud} + \frac{\tilde{j}_{\nu bg}}{\kappa_\nu} \right) (1 - e^{-\tau_\nu}) + I_{F,\nu} . \tag{5.10}$$

Here $I_{0bg,\nu}$ is the background intensity at the cloud position and $I_{F,\nu}$ is the foreground radiation intensity. The mean galactic background emission coefficient can be written in terms of the observed background intensity by considering a total length, D_{bg}, over which the emission occurs:

$$\tilde{j}_{\nu bg} \equiv \frac{I_{\nu bg}}{D_{bg}} . \tag{5.11}$$

$I_{0bg,\nu}$ can then be written as

$$\begin{aligned} I_{0bg,\nu} &= \tilde{j}_{\nu bg} \left(D_{bg} - (D_{cloud} + \frac{L_{cloud}}{2}) \right) \\ &\approx \tilde{j}_{\nu bg} \left(D_{bg} - D_{cloud} \right) , \end{aligned} \tag{5.12}$$

assuming $D_{cloud} \gg L_{cloud}/2$. The power received by an antenna of effective aperture A_{eff}, beam $B(\Omega)$ and having an operating bandwidth of $\Delta\nu$ (assuming flat response

over $\Delta\nu$) is (cf. Christiansen & Högbom)

$$P_{antenna} = \frac{1}{2}\Delta\nu A_{eff}\int_{4\pi} I_\nu(\Omega)B(\Omega)d\Omega\ . \tag{5.13}$$

Substituting for I_ν and converting the intensities into equivalent brightness temperature, we get

$$\begin{aligned} P_{antenna} &= \frac{kA_{eff}\Delta\nu}{\lambda^2}\Big[T_{0bg,\nu}\Omega_{cloud}e^{-\tau_\nu} \\ &\quad + T_{\nu bg}(\Omega_A - \Omega_{cloud}) + (T_e + \frac{T_M}{\tau_\nu})(1 - e^{-\tau_\nu})\Omega_{cloud} \\ &\quad + T_{F,\nu}\Omega_{cloud}\Big]\ . \end{aligned} \tag{5.14}$$

Here $\Omega_A = \int_{4\pi} B(\Omega)d\Omega$. An equivalent brightness temperature T_M is assigned to the radiation field inside the cloud due to the background by considering an intensity equal to $\tilde{j}_{\nu bg}L_{cloud}$. The antenna temperature T_A is defined using the equation

$$P'_{antenna} = kT_A\Delta\nu, \tag{5.15}$$

where the right-hand side is the noise power generated by a resistor kept at a temperature T_A over the bandwidth $\Delta\nu$. Substituting for $P_{antenna}$ and using the relation $\Omega_A = \lambda^2/A_{eff}$ we get

$$\begin{aligned} \Omega_A T_A &= T_{0bg,\nu}\Omega_{cloud}e^{-\tau_\nu} \\ &\quad + T_{\nu bg}(\Omega_A - \Omega_{cloud}) + (T_e + \frac{T_M}{\tau_\nu})(1 - e^{-\tau_\nu})\Omega_{cloud} \\ &\quad + T_{F,\nu}\Omega_{cloud}\ . \end{aligned} \tag{5.16}$$

The optical depth at the line frequency is given by $\tau_\nu = \tau_{C\nu} + \tau_{L\nu}$. The line temperature ΔT_L is the excess temperature above the continuum at a nearby frequency where $\tau_{L\nu} = 0$.

$$\begin{aligned} \Omega_A\Delta T_L &= T_{0bg,\nu}\Omega_{cloud}e^{-\tau_{C\nu}}(e^{-\tau_{L\nu}} - 1) \\ &\quad + T_e\left(\frac{b_m\tau^*_{L\nu} + \tau_{C\nu}}{\tau_{L\nu} + \tau_{C\nu}}(1 - e^{-(\tau_{L\nu}+\tau_{C\nu})}) - (1 - e^{-\tau_{C\nu}})\right)\Omega_{cloud} \\ &\quad + T_M\left(\frac{1 - e^{-(\tau_{L\nu}+\tau_{C\nu})}}{\tau_{L\nu} + \tau_{C\nu}} - \frac{(1 - e^{-\tau_{C\nu}})}{\tau_{C\nu}}\right)\Omega_{cloud}\ . \end{aligned} \tag{5.17}$$

Using this equation and the observed line parameters, it is possible, in principle, to constrain the physical properties for the ionized gas. The other unknown in the equation is the source angular size Ω_{cloud}.

5.3 Sensitivity of Low-Frequency RRL to Physical Conditions in the Ionized Gas

RRLs at low frequencies are sensitive to low density ionized gas (Shaver 1975). To illustrate this, let us consider four model clouds whose parameters are given in Table 5.1. Model 1 & 2 represent relatively high density clouds. Model 3 corresponds

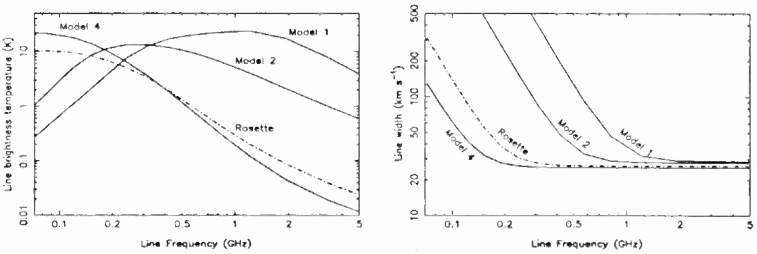

Figure 5.1: (a) The line brightness temperature of alpha transitions for hydrogen RRLs from the four model clouds (cloud parameters are given in Table 5.1) plotted as a function of the line frequency (left). (b) A plot of the width (FWHM) of line emission from the model clouds as a function of frequency is also shown (right).

Table 5.1: Physical parameters of the model clouds

Model	T_e (K)	n_e (cm^{-3})	EM (pc cm^{-6})	S (pc)	U (pc cm^{-2})	Comment
1	9000	500	6.0e5	2.4	151	H II region
2	8000	100	9.0e4	9.0	194	H II region
3	6000	10	3.0e3	30	139	Rosette nebula
4	5000	4.0	1200.0	75	189	H II envelope

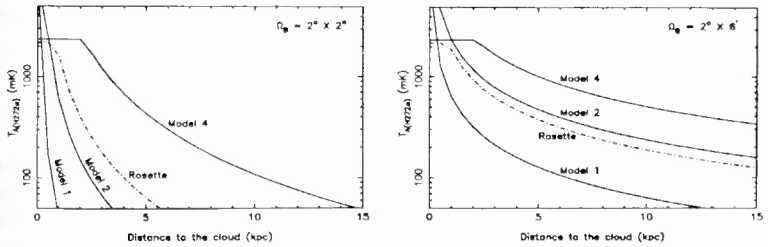

Figure 5.2: The line antenna temperature of H272α RRL transition from the four model clouds when observed with a beam (FWHM) of 2° × 2° (left) and 2° × 6′ (right) are plotted as a function of the line of sight distance to the cloud.

to the parameters of Rosette nebula taken from Celnik (1985). Model 4 corresponds to typical parameters for an H II region envelope derived by Anantharamaiah (1985b). The emission measures for models 1 and 2 are chosen such that the maximum excitation parameters fall in the range 100 – 200 pc cm^{-2}, which is typical for H II regions (Shaver & Goss 1970). The line brightness temperature of α–transitions of hydrogen RRLs from the model clouds are computed using Equation 5.17 and are plotted as a function of frequency in Fig. 5.1(a). For these computations we have assumed a temperature for the background emission of 1000 K at 327 MHz and a spectral index of -2.7. It is clear from Fig. 5.1(a) that the intrinsic line intensity peaks at lower frequencies if the density is low. This behavior implies that the low frequency observations are sensitive to ionized gas with parameters similar to models 3 and 4.

Another reason which favors detection of lines from low-density gas at low frequencies is due to relatively narrow width of line emission from such gas. Fig. 5.1(b) shows the computed width of line emission from the different models as a function of frequency. The line emission at low frequencies from high density gas have large widths due to pressure broadening (see Equation 5.3), which spreads out the energy of the line in the wings. Such weak and broad lines are difficult to observe because of the intrinsic baseline uncertainty in the spectral line system. This again implies that the low frequency observations favors detection of lines from ionized gas with parameters similar to models 3 and 4.

A question of interest is – what is the maximum line of sight distance to which the four model clouds can be detected given the sensitivity of observations discussed in this thesis ? Two modes of observations are presented in this thesis (see Section 2.4.1). These are observations with a 2° × 2° and 2° × 6′ beams. To study the sensitivity of observations to clouds at various distances, the antenna temperature of the H272α transition from the four model clouds as a function of the distance is computed. The computation is done for the two modes of observations and is shown in Fig. 5.2. The line antenna temperature is affected by: (a) the telescope beam and (b) the background emission at the cloud position. The sensitivity of our observations for a typical integration time of $\sim$ 20 hrs (background temperature = 1000 K, receiver temperature = 150 K, resolution bandwidth = 10 kHz) is about 95 mK. Thus Fig. 5.2 indicates that clouds

with parameter typical of H II envelopes can be detected (2 σ detection) to distances of about 7.5 kpc even with a beam of 2° × 2° beam. The higher angular resolution mode can detect clouds at even farther distances.

5.4 Physical Properties

The physical properties of the ionized region are obtained by computing the expected line emission as a function of frequency based on a simple model discussed in Section 5.2 and comparing them with the observed values. Several simplifying assumptions were made in the model. The line emission is assumed to originate from a single homogeneous ionized region characterized by an electron temperature T_e, density n_e and size S. Although this is an oversimplification, the available data does not warrant any more details about the regions. The angular extent of the ionized region is not determined observationally due to coarse angular resolution. This parameter is required to estimate the line brightness temperature from the observed line antenna temperature for comparison with the intensity predicted by the model. The line antenna temperature needs to be corrected by the factor $\frac{\Omega_B}{\Omega_{cloud}\eta_B}$ to get the line brightness temperature (see Equation 5.17), where Ω_{cloud} is the angular size of the line emitting region, η_B is the beam efficiency (= 0.65 for a module of the ORT; see Section 2.7.1) and Ω_B is the half power beam width. Observations near 327 MHz indicate that the angular extent of the cloud may be smaller than the beam (∼ 2° × 2°), at least in some cases, since the line intensity and the line profile changes significantly from one position to another which are separated by about 2° in longitude. Along the galactic latitude we have observations only at two specific longitudes ($l = 0°.0$, $13°.9$) which indicate that the line emission is extended in b over ∼ 1°.8 (FWHM). However examination of the line profiles at different latitudes at $l = 0°$ shows that the profile changes when the beam center is shifted by ± 1° along b. These changes indicate that the emission from an individual ionized region may have an angular extent less than 2° along galactic latitude. However, at $l = 13°.9$ the line emission appears to extend beyond ± 1° along b. Higher angular resolution (∼ 2° × 6′; see Section 6.6.1) observations towards some of the positions shows that the line emitting region may have an angular extent > 1°. Based on these observational facts we assume a cloud size of ∼ 1°.5 (along b) × 2° (along l) for modeling. The correction factor $\frac{\Omega_B}{\Omega_{cloud}\eta_B}$ for the low resolution observations ($\Omega_B = 2°.2$ (along N-S) × 2°.3 (along E-W)) is then ∼ 2.9. Since the beam width of the ORT is a function of declination (see Section 2.7), the factor $\frac{\Omega_B}{\Omega_{cloud}\eta_B}$ will be different for different directions. Another unknown quantity is the distance to the ionized region, which is required to estimate the background radiation intensity at its position (see Equation 5.17). For modeling, we considered both the "far" and "near" distance based on the observed central velocity of line emission. Nearer the galactic center ($|l|$ <4°) the peculiar motion of the ionized gas can dominate over the galactic differential velocity and hence the kinematic distance estimate is not reliable. Due to lack of better strategy we assumed that the ionized gas to be at about half the distance to the galactic center at these longitudes. The background radiation temperature at the location of the ionized region is then obtained by using the distance to the ionized region, the measured continuum temperature near 327 MHz and assuming a total column length for the radiation as 15 kpc (see Equation 5.17). The radiation temperature is scaled to different frequencies using a spectral index of −2.7.

5.4.1 Density of the Line Emitting Cloud

One important aspect of the interpretation of the RRL emission is that the density of the ionized gas is well constrained just from the recombination line observations near 1.4 GHz and 327 MHz (Anantharamaiah 1985b; see below). This is due to the markedly different dependence of line intensity on density at the two frequencies. We have used this aspect for estimating the density of the ionized gas at various observed positions. The 327 MHz data from the low resolution survey described in Chapter 3 is used for estimating the electron density. The RRL observations near 1.4 GHz are taken from Lockman (1976, 1980), Hart & Pedlar (1976b), Cersosimo (1990) and Heiles et al. (1996b). The HPBW of the observations of Lockman (1976, 1980) is 21′, Hart & Pedlar (1976b) is 31′ × 33′, Cersosimo (1990) is 34′ and Heiles et al. (1996b) is 36′ (also 21′ for the observations with the 140 ft telescope). All together there are about 274 positions observed in the longitude range of interest (i.e. 332° to 0° to 89°) and within $b = \pm 1°$. The beam sizes of all the above observations near 1.4 GHz are smaller than the angular resolution of 327 MHz observations. Therefore to obtain the line intensity near 1.4 GHz that would be observed with a beam similar to that of our observations, we followed the scheme described below. We selected the positions observed near 1.4 GHz that contain not more than two known H II regions within 50′ from the beam center and these H II regions should not have an angular size > 5′ as determined from their continuum emission at 5 GHz or 2.7 GHz. This criteria is used since the selected positions contain only H II regions which are compact and likely to be of higher density and hence do not contaminate the line emission near 1.4 GHz from the low-density gas. We used the data of Caswell & Haynes (1987), Lockman (1989) and Lockman et al. (1996) for identifying the H II regions. A total of 137 positions were selected. Using these data, composite spectra were constructed from all the observed spectra inside the ∼ 2° × 2° beam of our observations. The line parameters were then obtained from Gaussian fits to these composite spectra. If a composite spectrum contained multiple components, then the parameters of the component with central velocity nearest to that of the line detected at 327 MHz was used. Most of the positions (∼ 92 %) have only one component in the composite 1.4 GHz spectrum and the central velocity of the spectral feature matches within ± 5 km s^{-1} of the line observed near 327 MHz. The width of the line in some cases are however larger than that observed near 327 MHz. The peak line temperature obtained from the composite spectra is taken as the line brightness temperature near 1.4 GHz for modeling.

Table 5.2 gives the input parameters used for modeling. Column 1 gives the galactic longitude of the positions ($b = 0°$ for all positions) where data at both 327 MHz and 1.4 GHz are available, column 2 gives the line temperature near 1.4 GHz obtained from the composite spectra, column 3 gives the observed line antenna temperatures near 327 MHz, columns 4 and 5 give respectively the observed width and central velocity of the line emission near 327 MHz and the observed continuum brightness temperature near 327 MHz is given in column 6. The method used for constraining the density of the ionized gas is illustrated using the data at the position G11.6+0.0 (see Chapter 3). The modeling starts with the computation of the departure coefficient which are functions of the electron density and temperature. The departure coefficients are obtained by interpolating from a pre-computed table on a grid of electron temperatures and densities. The emission measure that is required to produce the observed line intensity is then obtained iteratively using Equation 5.17. The factor $\frac{\Omega_B}{\Omega_{cloud}\eta_B}$ (see Equation 5.17)

Table 5.2: Line and continuum parameters for modeling

l	T_L		ΔV	$V_{\rm LSR}$	T_C		
(b=0)	1.4 GHz	327 MHz	327 MHz		327 MHz	2.7 GHz	10 GHz
(^{o})	(mK)	(mK)	(km s^{-1})	(km s^{-1})	(K)	(K)	(K)
332.1	43	133	47.8	−58.4	239		
340.3	50	120	54.1	−36.3	291		
357.6	23	291	26.2	−1.2	663		
0.0	102	664	29.0	5.9	1007	7.2	0.47
2.3	13	209	26.0	10.2	649	3.7	0.10
4.7	26	378	28.8	11.3	598	3.5	0.07
7.0	29	347	24.8	20.6	636	4.1	0.14
9.3	24	255	33.9	19.6	579	3.6	0.11
11.6	35	269	43.0	27.2	548	3.4	0.10
13.9	27	513	38.1	26.9	610	4.1	0.19
16.1	46	375	46.6	28.8	528	4.0	0.14
18.4	31	298	30.6	30.0	557	3.4	0.13
20.7	17	142	34.2	55.2	501	3.0	0.11
36.5	21	107	60.0	65.2	378	2.3	0.08
41.0	13	59	36.3	55.1	323	1.8	0.05
45.5	12	60	40.5	48.8	248	1.4	0.04
50.0	14	52	58.3	50.5	250	2.1	0.12
54.6	9	41	14.2	31.4	139	1.0	
59.2	11	39	21.0	25.2	101	0.8	
61.5	10	38	34.9	29.4	97	0.8	
63.8	13	38	14.7	22.6	81	0.7	
73.3	9	30	29.1	22.6	80	1.0	
75.8	12	44	39.9	3.4	97		
78.2	45	125	35.1	3.1	170		
80.7	64	142	28.5	4.1	172		
83.3	58	75	37.8	3.8	105		

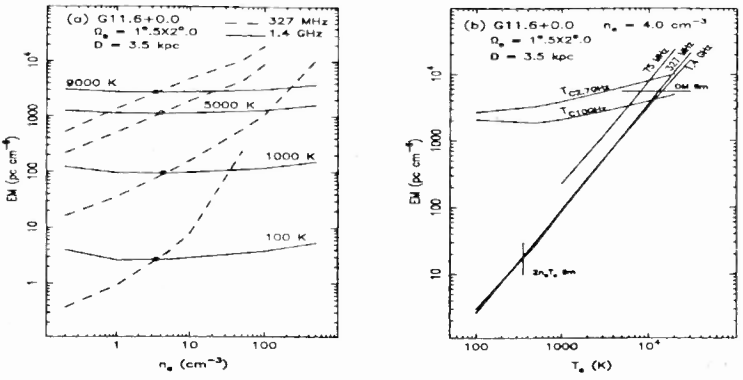

Figure 5.3: Constraining the physical properties of the gas producing RRL emission near 327 MHz towards the direction $l = 11°.6$ and $b = 0°.0$. The plots are made for the case when the clouds are placed at the near kinematic distance of 3.5 kpc. (a) Plot of the emission measure required to produce the observed line intensity as a function of electron density at 4 different temperatures as marked. The dashed lines are for line emission near 327 MHz and the continuous lines are for the 1.4 GHz line emission. It is clear that the density of the gas, defined by the intersection point of the two curves, is well constrained at about 4.0 cm^{-3} for any temperature. (b) Various constraints on the combination of emission measure and electron temperature of the ionized region (see text). The density as determined from (a) is used.

for this direction is estimated as 3.0. The Doppler width, which appears in Equation 5.17 through the expression for line optical depth, is computed as follows. For a given combination of electron density and temperature, the line width due to pressure broadening is computed using Equation 5.3. The Doppler width is then obtained from Equation 5.4 using the observed line width and the computed width due to pressure broadening. The background radiation temperature *at the cloud position* is obtained as discussed in Section 5.2. For this example, we have taken the "near" distance which is 3.5 kpc. Fig 5.3a shows a plot of the estimated emission measure as a function of density for various temperatures. At each electron temperature, the intersection point of the curves corresponding to RRLs at 1.4 GHz and 327 MHz give the density of the gas. It is remarkable that the electron density is determined within a factor of two regardless of the temperature and emission measure. The uncertainties in the estimated density are due to (a) the cloud angular size considered for the analysis (b) the assumption that the galactic background radiation has a uniform emissivity and (c) error in the estimated distance.

The density of the ionized gas is estimated for different positions using the method described above and is given in Column 4 of Table 5.3. The galactic longitude, the factor $\frac{\Omega_{cloud}\eta_B}{\Omega_B}$ used to convert the observed line antenna temperature near 327 MHz to line brightness temperature and the kinematic distance are given in columns 1, 2 and 3 respectively of Table 5.3. The derived densities of the line emitting regions are in the

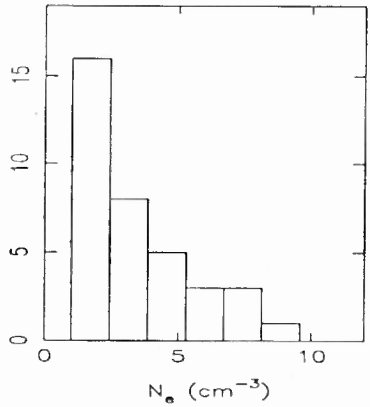

Figure 5.4: Histogram of the derived electron density of the ionized gas producing the RRL emission near 327 MHz. The estimated densities for both 'far' and 'near' distances are used to obtained this plot.

range of 1 – 10 cm^{-3} . Fig. 5.4 shows the histogram of the derived electron densities. These values are consistent with the earlier estimates of the physical properties of the low density gas in the galactic plane by Anantharamaiah (1985b, 1986).

5.4.2 Constraining the Temperature and the Size of the Ionized Region

It is not possible to estimate the temperature and the size of the line emitting region just from the 327 MHz and 1.4 GHz data (Anantharamaiah 1985b). This is clear from Fig. 5.3b for the data at position G11.6+0.0. In this figure, using the density as determined above, the emission measures required for producing the measured RRL intensity near 1.4 GHz and 327 MHz are plotted as a function of electron temperature. A large range of emission measures and a correspondingly large range of temperatures can produce the observed line intensity at the two frequencies. We tried to use the upper limits on hydrogen line emission near 75 MHz to constrain the temperature and size. The upper limit for the line to continuum ratio near 75 MHz is $\sim 10^{-4}$ (Erickson et al. 1995) in the longitude range $|l|$ <20°. The upper limit on the line brightness temperature was estimated from this ratio using the continuum temperature near 75 MHz and taking 0.2 ($\sim \frac{1^\circ.5 \times 2^\circ}{4^\circ \times 4^\circ}$, $4^\circ \times 4^\circ$ is the beam size used for observations at 75 MHz) as the value for the factor $\frac{\Omega_{cloud} \eta_B}{\Omega_B}$. However, we found that this upper limit could not narrow down the allowed ranges of electron temperature and size (see Fig 5.3b). The parameter space to the right of the 75 MHz curve is consistent with the upper limit and thus could only provide a cross check on the consistency of the model obtained from the 1.4 GHz and 327 MHz lines.

In directions where the model is consistent with all the RRL observations, upper limits on the electron temperature and the size of the line emitting region were estimated

using other criteria. These criteria are (1) the line width, (2) continuum emission from the ionized region (3) the dispersion measure (DM) produced by the region and (4) the thermal pressure of the ionized gas. The first three criteria can provide upper limits on the electron temperature. The line width due to Doppler broadening cannot exceed the observed line width if we assume that the broadening is purely because of thermal motions, thus providing an upper limit to the temperature. This upper limit is significant at positions where narrow (< 15 km s^{-1}) lines were observed. The ionized gas responsible for RRL emission also produces continuum emission, the intensity of which is a function of electron temperature and emission measure (see Eq. 5.5). The measured continuum at the observed positions have contribution from both thermal emission from the cloud and non-thermal emission from the galactic background. At frequencies higher than a few GHz, a good fraction of the continuum emission (~ 50 % at 10 GHz in the inner Galaxy, Brodbent, Haslam & Osborne 1989) is thermal and hence the measured continuum temperature at these frequencies can be used to constrain the physical properties of the line emitting region. The measured continuum temperature can have contribution from the non-thermal background emission as well as from other ionized components, which are not detected in RRLs near 327 MHz, and thus can only provide an upper limit to emission from the ionized gas producing the observed RRLs. The continuum temperature towards the observed positions near 2.7 GHz and 10 GHz were obtained from the maps of Reich et al. (1990) and Handa et al. (1987). To get an average continuum temperature towards the observed positions, both these maps were convolved with a beam comparable to the resolution of the 327 MHz RRL survey. The continuum temperatures thus obtained for these frequencies are given in Table 5.2 (columns 7 & 8). For the data at the position G11.6+0.0, the cloud parameters that can produce the observed continuum temperatures are indicated by two curves marked in Fig. 5.3b. The intersection of these curves with that obtained from RRL observations gives an upper limit to the temperature and thus an upper limit to the size of the line emitting region.

Study of the dispersion of pulsar signals give the column density of electrons along the line of sight to the pulsars in the Galaxy. Analysis of DM measured towards pulsars of known distances was used by Taylor & Cordes (1993) to construct a free-electron density model of the Galaxy. This model can be used to estimate the DM in a given direction in the Galaxy, which in turn can be used to constrain the properties of ionized gas responsible for RRL emission. The DM due to the ionized gas that produces the observed RRLs should be less than that obtained from the electron density model of Taylor & Cordes (1993). The DM in an observed direction is obtained from the electron density model by considering a galactic disk of radius 10 kpc and integrating the electron density over the line of sight to the end of the disk. The upper limits on the electron temperature and size obtained towards G11.6+0.0 using this criteria is shown in Fig. 5.3b. The DM estimated from the electron density model in this direction is $\sim$ 1300 pc cm^{-3} .

A lower limit on the temperature of the ionized gas can be obtained by considering that the thermal pressure ($\sim 2n_e kT_e$) due to the gas should be greater than the mean ISM pressure, which is $\sim 3000k$ K cm^{-3} , where k is the Boltzmann factor. This lower limit for the data at the position G11.6+0.0 is shown in Fig. 5.3b. We found that in most cases the lower limits obtained from the thermal pressure considerations are too small to give any meaningful limit.

The range of physical parameters for the ionized regions obtained using the above

Table 5.3: Physical properties

l				S	Upper limit		
$b = 0°$	$\frac{\Omega_s \eta_B}{\Omega_B}$	D	n_e	T_e = 7000 K	T_e	S	Note
(°)		(kpc)	(cm^{-3})	(pc)	(K)	(pc)	
332.1	0.14	4.1	2.2		6900	530	a
332.1	0.14	10.9	1.2		3900	1000	a
340.3	0.18	3.1	7.4	60	14500	180	a
340.3	0.18	12.9	2.6		6400	520	a
357.6	0.30	4.2	1.8	215	13400	650	a
0.0	0.31	4.2	8.6	45	15500	155	a
2.3	0.31	4.2	1.4	235	14600	870	b
4.7	0.32	3.1	1.6	340	11000	700	a
7.0	0.32	3.9	2.2	180	13300	540	b
9.3	0.33	3.0	2.7	130	15000	470	a
11.6	0.33	3.5	4.9	80	11400	170	c
16.1	0.34	2.8	4.7	115	11700	260	c
18.4	0.34	2.7	3.5	95	17300	430	a
20.7	0.34	4.4	3.4	65	22000	440	a
20.7	0.34	11.5	1.1	700	10700	1300	a
36.5	0.35	4.5	7.0	35	10000	60	c
36.5	0.35	9.2	4.0	110	9700	180	c
41.0	0.35	3.7	6.5	15	15400	50	c
41.0	0.35	9.1	3.3	60	15100	210	a,c
45.5	0.34	3.3	4.0	40	16800	185	c
45.5	0.34	8.6	2.1	155	11800	350	a
50.0	0.34	4.0	7.9	20	14300	55	a
50.0	0.34	6.9	5.9	35	11800	70	a
54.6	0.33	2.3	2.6		4400	15	b
54.6	0.33	7.5	1.5		4400	45	b
59.2	0.32	2.0	2.9	40	9500	70	b
59.2	0.32	6.7	1.8	115	9500	200	a,b
61.5	0.32	2.9	2.2	100	8900	150	a
61.5	0.32	5.2	1.8	170	7600	190	a
63.8	0.31	2.1	2.8		4700	20	b
63.8	0.31	5.4	2.2		4700	35	b
73.3	0.23	1.2	1.4	200	7600	230	a
73.3	0.23	3.6	1.2		6600	280	a
75.8	0.22	4.0	1.2		4500	260	a
78.2	0.21	3.3	4.1		5000	80	a
80.7	0.20	2.6	5.6		5600	55	a
83.3	0.19	1.9	12.0	20	8100	25	a

Note : a – limit from DM; b – limit from line width; c – limit from 10 GHz continuum.

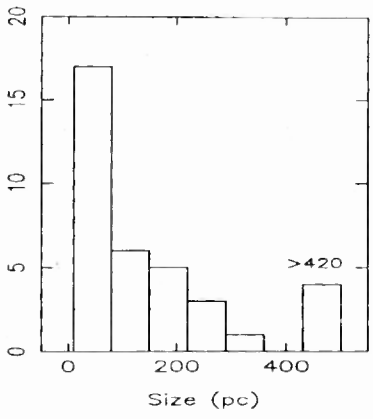

Figure 5.5: Histogram of the estimated path lengths of the ionized gas producing the RRL emission near 327 MHz. The temperature of the ionized gas is taken as 7000 K. The upper limits on the path lengths for positions where the maximum allowable temperature is less than 7000 K are also included in the histogram.

criteria is large. This large range is clear from Fig. 5.3b for the case of G11.6+0.0. Thus the temperature and size could not be well constrained from the presently available observations. We therefore estimated the required path length for producing the observed line emission by assuming a temperature of 7000 K for the ionized gas. This value is close to the mean temperature of H II regions near the solar circle as determined by Shaver et al. (1983). It is also consistent with the temperature obtained by Heiles et al. (1996b) for the low-density ionized gas from RRL observations near 1.4 GHz. The estimated path lengths for the assumed temperature are given in column 5 in Table 5.3. The estimated path lengths are in the range of 20 – 200 pc. Fig. 5.5 shows the histogram of the estimated path lengths. These values are comparable to the estimates by Anantharamaiah (1985b). The derived upper limits on electron temperature and size are given in columns 6 and 7 respectively. The criterion that resulted in the upper limits is given in column 8. The upper limit for temperature is typically 10000 K and that for the path length is typically 600 pc.

In the longitude range $l = 75°$ to $83°$, the "near" distances obtained from the central velocity of RRL emission are less than 1 kpc. The interstellar extinction at these distances is < 2 mag (Hakkila et al. 1997). Therefore the Hα emission from the ionized gas producing RRLs should be observable. However, the Hα intensity obtained from the models with "near" distance in these longitudes are higher than the values observed by Reynolds (1983). For these estimates, we used the A_v values from Hakkila et al. (1997) to account for the attenuation of Hα photons due to interstellar extinction. We therefore conclude that the ionized gas responsible for RRL emission in the longitude range $75° < l < 83°$ are likely to be at the "far" distance. For these positions, modeling was done assuming the "far" distance.

The main results of the simple modeling described above can be summarized as

follows.

1. The derived densities of the line emitting regions are in the range of $1 - 10\ cm^{-3}$.

2. For a few positions, the temperature of the line emitting region is constrained by the observed line width. The upper limits thus obtained are, in some cases, $<$ 4800 K. These regions may be similar to the low temperature H II regions reported earlier by Shaver et al. (1979), Lockman (1989) and Lockman et al. (1996).

3. The estimated path lengths for the line emitting regions for a temperature of 7000 K and the upper limits for the path lengths for the positions where the maximum allowable temperatures are less than 7000 K are in the range of 20 – 200 pc.

4. In the longitude range $l = \pm 20°$, no model consistent with the 75 MHz upper limit could be obtained when the ionized gas is placed at the "far" distance. An exception is G340.3+0.0.

5. For the position G13.9+0.0, no solution which is consistent with the 75 MHz upper limit could be obtained.

5.5 Comparison with other Related Observations

The widespread presence of low-density ionized gas in the inner Galaxy is evident from other observations as well. These observations were summarized in section 1.3. They include (a) absorption of the galactic non-thermal background radiation in the inner Galaxy at frequencies $<$ 100 MHz (Westerhout 1958, Shain et al. 1961, Mathewson et al. 1962, Brodbent et al. 1989, Dwarakanath 1989) and (b) observation of wide spread emission of diffuse N II 205 μm and C II 158 μm fine structure transitions in the galactic plane (Wright et al. 1991, Nakagawa et al. 1998). In this section we use the derived electron density and the estimated path lengths for an assumed temperature of 7000 K (wherever upper limits on T_e exceed 7000 K) to estimate the expected intensities of N II 205μm , C II 158μm and Hα lines from the ionized gas. The absorption of the galactic background emission near 34.5 MHz due to this low-density ionized gas is also estimated using these parameters. Where the maximum allowable temperature for the model is less than 7000 K, upper limits on the path lengths and T_e are used for the computation. The estimated values are compared with results from existing observations.

5.5.1 Galactic Background Emission near 34.5 MHz

Our aim is to estimate the effect of the low-density ionized gas on the non-thermal background radiation near 34.5 MHz and compare it with the observed brightness temperature. The expected brightness temperature near 34.5 MHz in the absence of such ionized clouds can be estimated approximately using the measured temperature at 408 MHz (Haslam et al. 1982) which can be scaled to 34.5 MHz using a spectral index of -2.7 (Salter & Brown 1988). Any ionized cloud along the line of sight attenuates the background radiation by a factor $e^{-\tau_c}$ where τ_c is the free-free optical depth. The net observed radiation intensity also has an un-attenuated contribution from the foreground. The net observed radiation intensity is computed using a simple model where

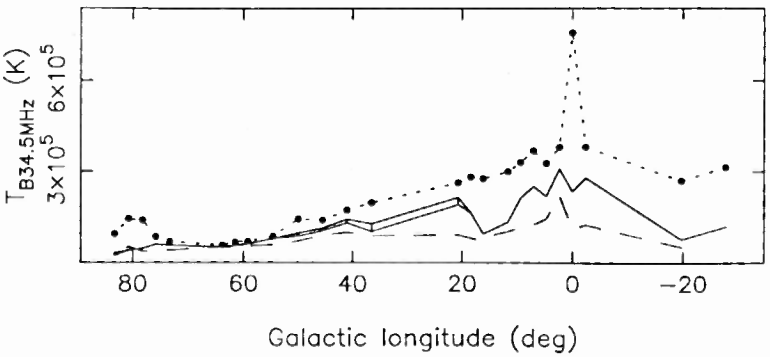

Figure 5.6: Plot of the estimated range of the continuum brightness temperature near 34.5 MHz (continuous line) in the presence of ionized clouds producing RRLs near 327 MHz as a function of galactic longitude. At positions where the physical properties are available when the ionized gas is at the "near" and "far" distances the continuum brightness temperatures corresponding to the two cases are estimated. The two values of brightness temperature for these positions are also marked in the plot. The continuum temperature scaled to 34.5 MHz from 408 MHz values using a spectral index of -2.7 is shown as a dotted line. The observed continuum near 34.5 MHz taken from Dwarakanath & Udayashankar (1990) is shown as dashed line.

the ionized region is placed at a distance D_c from Sun. The distance D_c is constrained by the observed LSR velocity of RRL emission. We assume that the ionized region is homogeneous and has an angular size of 1°.5 (along b) × 2° (along l). The background and foreground non-thermal emission is computed by assuming that its emissivity is uniform in the galactic disk. The total column length D in a given direction is obtained by considering a galactic disk of radius 15 kpc. Using the solution of the radiative transfer equation, the observed brightness temperature T_o can then be written as

$$T_o(\nu) = \frac{T_{sky}(\nu)}{D}(D - D_c)e^{-\tau_c} + T_e(1 - e^{-\tau_c}) + \frac{T_{sky}(\nu)}{D}D_c \qquad (5.18)$$

where T_e is the electron temperature, $T_{sky}(\nu)$ is the observed background brightness temperature in the absence of the cloud. $\frac{T_{sky}(\nu)}{D}(D - D_c)$ and $\frac{T_{sky}(\nu)}{D}D_c$ are the contribution to the net brightness temperature from behind and in front of the cloud respectively.

Fig. 5.6 shows the estimated galactic background brightness temperature near 34.5 MHz as a function of the galactic longitude in the presence of the low-density ionized gas. The measured brightness temperatures near 34.5 MHz and the temperature scaled from 408 MHz observations are also plotted in the figure. The brightness temperature near 34.5 MHz are obtained from the continuum map of Dwarakanath & Udayashankar (1990). The brightness temperature near 34.5 MHz and the temperature scaled from 408 MHz observations are obtained after convolving the respective continuum maps to an angular resolution of 1°.5 × 1°.5. The average decrement in the continuum

temperature as obtained from the modeling (i.e. $1 - T_o/T_{sky}$) in the longitude range $l = 340°$ to $0°$ to $84°$ is ~ 37 % while the observed value is ~ 56 %. Thus it is clear (see also Fig. 5.6) that although the absorption of the background radiation due to the low-density ionized gas is significant, it does not account for all the observed absorption. Our model, however, assumes the presence of a single low density ionized cloud which is responsible for RRL emission near 327 MHz along each line of sight. In reality there are other forms of ionized gas present in the galactic disk which can contribute to the continuum absorption at low frequencies. For example, the ionized gas responsible for optical nebulosities cataloged by Rodgers et al. (1960) and Sivan (1974) can add to the continuum absorption (Dwarakanath 1989). Other limitations of our model are: (a) the background temperature at the cloud position is estimated by assuming an uniform emissivity for the galactic non-thermal radiation, (b) there is some uncertainty in the physical properties of the low density ionized gas (see Table 5.3) and (c) the distances to the ionized gas is not well determined.

5.5.2 C II and N II Emission from the Galactic Plane

For a temperature of 7000 K, the critical density below which C II and N II transitions can occur are ~ 30 cm^{-3} and ~ 150 cm^{-3} respectively (Osterbrock 1989). The derived densities of the ionized gas responsible for the RRL emission are much smaller than these critical densities. We therefore explore the possibility that the fine structure lines are produced in the same ionized region that are responsible for RRL emission near 327 MHz.

The equations used for the computation of the fine-structure line intensities are (Heiles 1994)

$$I_{\rm C\,II} = 1.55 \times 10^{-7} \delta_{C+} T_e^{-0.35} n_e^2 L \quad (5.19)$$

$$I_{\rm N\,II} = 1.55 \times 10^{-9} \delta_{N+} T_e^{-0.5} n_e^2 L \quad (5.20)$$

where the $I_{\rm C\,II}$ and $I_{\rm N\,II}$ are the intensities (ergs cm^{-2} s^{-1} sr^{-1}) of C II 158μm and N II 205μm transitions respectively, δ_{C+} and δ_{N+} account for depletion onto dust grains or other ionization states of C and N respectively, T_e is the electron temperature in units of 10^4 K, n_e is the electron density in çm^{-3} and L is the path length in pc. These equations are good approximations for temperatures in the range 4000 – 10000 K and densities much less than the critical density. Cosmic abundances of C/H $= 4 \times 10^{-4}$ and N/H $= 1 \times 10^{-4}$ are assumed for obtaining the equations. We have used depletion factors of 0.5 for C and 0.78 for N for the computation of line intensities (Heiles 1994). Fig. 5.7 shows the plot of the estimated line intensities of the fine-structure transitions of C II and N II as a function of galactic longitude using the value of the physical properties of the ionized gas given in Table 5.3. The intensities of these lines measured with the *COBE*'s Far Infrared Absolute Spectrophotometer (FIRAS) (Wright et al. 1991) are also plotted in the figure. The *COBE* FIRAS measurements were averaged over a beam of $7° \times 5°$. Thus it is not possible to do a quantitative study at this stage. It is however clear that the estimated intensities are comparable to the *COBE* FIRAS measurements indicating that most of N II and C II emissions could originate in the low-density ionized gas which is responsible for the RRL emission observed near 327 MHz.

Accurate LSR velocity measurements of the fine-structure lines are not yet available for all the directions in the inner Galaxy. Results of Balloon borne observations of C II 158μm transitions from the galactic plane in the longitude range $-10°$ to $25°$ are

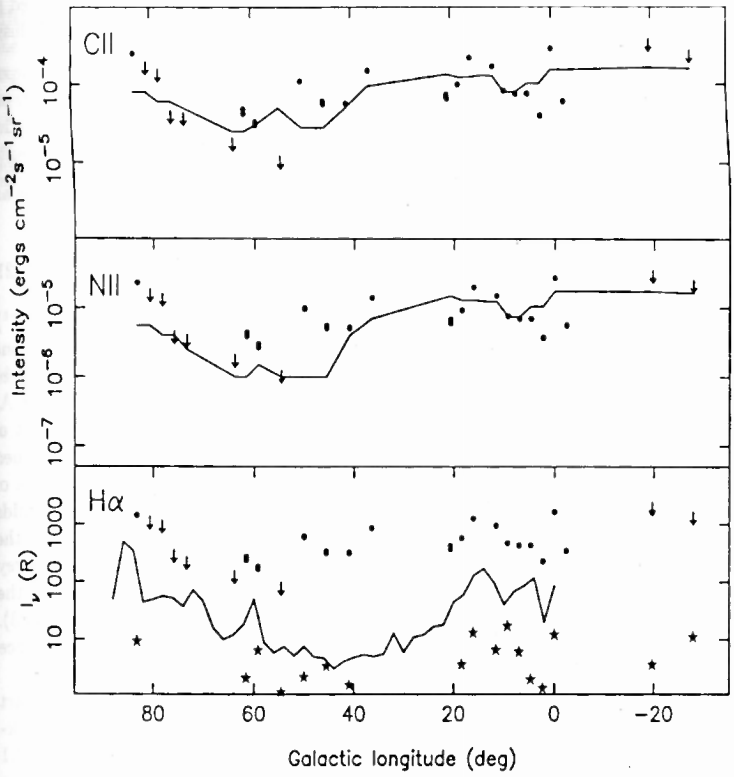

Figure 5.7: The estimated far infrared fine structure line emission and the Hα emission from the ionized clouds which produce the RRL emission near 327 MHz in the inner Galaxy. The computed values are marked by dots and the arrows represent upper limits. The expected Hα intensity after applying estimated interstellar extinction are shown as stars. The solid line are the measured line emission at different positions. The C II and N II line intensity are from the *COBE* FIRAS measurements (Wright et al. 1991), which are an average over a beam of 7° × 5°. The Hα measurements are taken from Reynolds (1983).

presented by Nakagawa et al. (1998). The angular resolution of these observations are 15′. The *lv* diagram obtained from this data shows a good similarity with that obtained from the RRL observations in the galactic plane. Thus we conclude that a considerable amount of the observed C II lines originate in the low-density ionized gas which is responsible for the RRL emission at 327 MHz and 1.4 GHz. This conclusion is consistent with the suggestion by Heiles (1994).

5.5.3 Hα Emission

In this section we compare the estimated Hα emission from the RRL emitting low-density ionized gas with observations of Hα by Reynolds (1983). The Hα intensities are computed using the equation (Heiles 1994)

$$I_{H\alpha} = 0.36 T_e^{-0.9} n_e^2 L \tag{5.21}$$

where $I_{H\alpha}$ is the intensity of Hα emission in Rayleigh ($= 2.4 \times 10^{-7}$ ergs cm^{-2} s^{-1} sr^{-1}), T_e is the electron temperature in units of 10^4 K, n_e is the electron density in cm^{-3} and L is the path length in pc. The observable intensity of Hα emission will however be less than the computed values because of interstellar extinction. We have used the A_v obtained from the visual extinction model of Hakkila et al. (1997) to take account of this attenuation. The Hα intensity computed using Equation 5.21 and that obtained after applying the attenuation due to interstellar extinction are plotted as a function of galactic longitude in Fig. 5.7. For comparison, the observed values taken from Reynolds (1983) are also plotted. It is clear from Fig. 5.7 that most of the Hα emission from the ionized gas producing RRL emission near 327 MHz is not observed in the Hα survey of Reynolds (1983) due to large interstellar extinction. In few of the positions the computed Hα intensity is above 5 σ detection limit of the survey (Reynolds 1983). However, the observations of Reynolds (1983) do not sample these positions and hence a direct comparison could not be made.

The lines detected in the Hα survey consists of emission from discrete regions apart from a fainter, smoothly varying Hα background (Reynolds 1983). The smooth background emission originate from ionized gas with an RMS electron density of ~ 0.1 cm^{-3} and is extended within ~ 1 kpc from the Sun. The 327 MHz RRL survey is not sensitive enough to detect radio recombination lines from this gas. RRLs from discrete ionized regions producing Hα emission are detectable in some cases (Reynolds 1983). However in most directions either the sensitivity of the RRL observations or the interstellar extinction make it difficult to detect both Hα and radio lines from the same ionized gas. Thus the RRL observations complement the Hα survey.

5.6 Summary

In this chapter we combined our data with other existing observations to constrain the physical properties of the ionized gas responsible for RRL emission near 327 MHz. The derived electron densities of the ionized gas are in the range 1 – 10 cm^{-3} . The upper limits obtained for the temperatures and sizes of the line emitting regions, from considerations of DM, continuum temperatures at 2.7 GHz and 10 GHz and the line widths, are typically $T_e \sim 10000$ K and $S \sim 600$ pc. The path lengths through the regions assuming an electron temperature of 7000 K are in the range 20 – 200 pc.

Using the derived physical properties, we estimated the expected C II 158 μm and N II 205 μm line emission from these low-density ionized regions. We found that most of the N II emission and a considerable fraction of the C II emission observed by the *COBE* satellite could originate in the same ionized gas which is responsible for the RRL emission. The Hα emission from these ionized gases is mostly not detectable in the existing Hα surveys due to large interstellar extinction. We also computed the expected free-free absorption of the galactic non-thermal emission near 34.5 MHz due to the presence of these ionized clouds. We found that a considerable fraction, if not all, of the absorption of the background radiation at low frequencies < 100 MHz could be due to the low density ionized gas which is responsible for the observed RRL emission near 327 MHz.

Chapter 6

Recombination Line Observations using a $2^\circ \times 6'$ Beam

6.1 Introduction

The low-resolution ($2^\circ \times 2^\circ$) survey of the RRLs in the galactic plane, which was described in Chapter 3, detected the hydrogen lines in almost all directions in the inner Galaxy. The observed line emission as a function of galactic longitude shows large fluctuations indicating that the line emitting region may be clumpy. Higher resolution observations of the line emitting region for studying the nature of the clumpiness are presented in this chapter. A selected set of fields that were observed in the low resolution ($2^\circ \times 2^\circ$) survey were observed with the $2^\circ \times 6'$ beam of the ORT. A total of about 252 spectra were obtained in these observations. The $2^\circ \times 6'$ beam is achieved by adding the signals in phase from all the 22 modules of the ORT.

6.2 Observations and Results

The observations described in this chapter are made in Mode B as described in Chapter 2 (Section 2.4.1). Since it is extremely time consuming to make a complete sampling of the galactic plane with the $2^\circ \times 6'$ beam, we selected a set of nine fields of widths 2° and 6° in the inner Galaxy. Hydrogen lines were detected in the low resolution survey towards all these fields. Table 6.1 gives the summary of the observations and parameters derived from the line profiles shown in Figs. 6.5 to 6.18. Column 1 & 2 are the galactic longitude and latitude of beam centers of the observed positions respectively. The ratio of line temperature to system temperature, the line width and the central velocity with respect to LSR are given in columns 3, 4 and 5 respectively, the velocity resolution to which the final spectra (shown in Fig. 6.5 to 6.18) are smoothed is given in column 6, the R.M.S noise in units of T_L/T_{sys} is given in column 7, the effective integration on each position is given in column 8 and the note in column 9 indicate tentative detections. Figs. 6.5 to 6.18 show the observed spectra towards the nine fields. The y-axis of all the spectra are in units of T_L/T_{sys}. Typical effective integration time on each position is $\sim$ 9 hrs.

Hydrogen lines were detected in almost all positions in the fields with $l < 35^\circ$. In several cases, the line parameters seem to vary when the beam center is moved by $6'$ in declination. For example, the width of the lines detected towards G347.78−0.14 and

Table 6.1: Summary of observations with the 2° × 6′ beam

l (^{o})	b (^{o})	T_L/T_{sys} × 10^3	ΔV (km s^{-1})	$V_{\rm LSR}$ (km s^{-1})	V_{res} (km s^{-1})	RMS[1] × 10^3	t_{int} (hrs)	Note
Field 1 (G348.0+0.0)								
347.22	−0.56				8	0.14	6.9	
347.30	−0.50				5	0.19	7.1	
347.38	−0.44	0.55(0.02)	31.4(1.5)	−9.8(0.6)	8	0.15	8.1	
347.46	−0.38	0.47(0.02)	39.4(2.3)	−16.1(1.0)	8	0.12	13.8	
347.54	−0.32	0.50(0.03)	22.0(1.5)	−11.5(0.6)	5	0.14	12.2	
347.62	−0.26	0.58(0.05)	29.3(2.7)	−11.7(1.1)	5	0.16	12.5	
347.70	−0.20	0.61(0.03)	11.0(0.7)	−11.7(0.3)	5	0.13	14.2	
347.78	−0.14	0.53(0.01)	37.5(1.1)	−13.3(0.5)	8	0.10	16.3	
347.86	−0.08	0.52(0.02)	33.3(1.4)	−1.4(0.6)	8	0.12	9.5	
347.94	−0.02	0.61(0.03)	35.7(2.2)	−13.1(0.9)	8	0.17	6.9	
348.02	+0.03	0.48(0.02)	46.1(2.2)	−15.6(0.9)	8	0.14	10.3	
348.10	+0.09	0.63(0.02)	31.0(1.1)	−14.5(0.4)	8	0.10	13.6	
348.18	+0.15	0.64(0.02)	39.7(1.5)	−15.4(0.6)	8	0.13	10.7	
348.26	+0.21	0.62(0.02)	29.6(0.9)	−19.0(0.4)	8	0.13	15.0	
348.42	+0.33				8	0.24	11.3	
348.51	+0.39	0.63(0.03)	34.9(2.0)	−18.1(0.8)	8	0.12	13.2	
348.67	+0.51	0.55(0.02)	32.4(1.6)	−18.3(0.7)	8	0.14	9.7	
348.75	+0.57	0.72(0.03)	31.8(1.5)	−16.1(0.6)	8	0.13	11.5	
Field 2a								
0.43	−0.02	0.84(0.03)	40.8(1.8)	3.3(0.8)	8	0.17	10.2	
0.52	+0.03	0.64(0.02)	44.2(1.6)	−2.3(0.7)	8	0.11	12.8	
0.67	−0.00	0.53(0.02)	33.1(1.7)	4.8(0.7)	8	0.11	11.2	
0.75	+0.05	0.77(0.04)	34.0(1.9)	0.2(0.8)	8	0.14	11.6	
0.84	+0.10	0.72(0.02)	22.4(0.9)	4.5(0.4)	8	0.11	9.4	
0.92	+0.16	0.78(0.03)	23.7(1.0)	5.1(0.4)	8	0.11	12.6	
Field 2b (G2.3+0.0)								
1.12	+0.02	0.52(0.02)	40.4(1.6)	0.4(0.7)	8	0.13	10.2	
1.21	+0.07	0.58(0.02)	45.9(1.9)	−4.3(0.8)	8	0.10	10.3	
1.29	+0.13	0.40(0.02)	42.8(3.0)	−0.3(1.2)	8	0.12	9.9	
1.38	+0.18	0.52(0.02)	41.9(2.1)	5.4(0.9)	8	0.12	10.1	
1.58	+0.04	0.66(0.02)	28.3(1.3)	2.1(0.5)	8	0.13	11.8	
1.66	+0.09	0.48(0.02)	37.8(2.3)	6.5(0.9)	8	0.12	12.2	
1.75	+0.14	0.33(0.03)	25.9(2.5)	3.2(1.1)	8	0.13	11.1	t
1.83	+0.20	0.51(0.03)	36.1(2.2)	7.8(0.9)	8	0.13	11.3	
2.03	+0.06	0.57(0.02)	28.4(1.2)	1.0(0.5)	8	0.13	12.0	
2.12	+0.11	0.46(0.03)	21.9(1.6)	3.6(0.7)	8	0.13	12.4	
2.21	+0.16	0.43(0.02)	31.9(2.2)	1.2(0.9)	8	0.11	14.8	
2.29	+0.21	0.57(0.02)	21.0(1.4)	11.9(0.6)	8	0.10	14.9	

Table 6.1: *Continued*

l (^{o})	b (^{o})	T_L/T_{sys} $\times 10^3$	ΔV (km s^{-1})	$V_{\rm LSR}$ (km s^{-1})	V_{res} (km s^{-1})	RMS[1] $\times 10^3$	t_{int} (hrs)	Note
2.54	−0.03				8	0.18	8.1	
2.63	+0.02	0.44(0.02)	42.2(2.3)	6.9(1.0)	8	0.11	11.2	
2.78	−0.03	0.64(0.02)	34.7(1.2)	7.8(0.5)	8	0.09	11.2	
2.86	+0.02	0.44(0.02)	28.2(1.8)	8.5(0.8)	8	0.11	12.5	
3.01	−0.03	0.65(0.03)	27.5(1.4)	5.2(0.6)	8	0.12	11.2	
3.09	+0.02	0.40(0.03)	21.4(1.8)	7.2(0.8)	8	0.11	11.7	t
3.24	−0.03	0.46(0.01)	34.5(1.3)	5.9(0.5)	8	0.15	10.1	
3.33	+0.02	0.40(0.02)	26.7(2.0)	8.6(0.8)	8	0.11	11.5	
			Field 2c (G4.7+0.0)					
3.47	−0.03	0.36(0.02)	33.6(2.4)	7.9(1.0)	8	0.13	9.2	t
3.56	+0.02	0.57(0.02)	24.7(0.9)	12.5(0.4)	8	0.09	10.4	
3.71	−0.03	0.69(0.03)	27.0(1.3)	8.4(0.5)	8	0.14	8.8	
3.79	+0.02	0.49(0.02)	34.4(2.0)	4.0(0.8)	8	0.12	11.6	
3.94	−0.03	0.66(0.04)	18.3(1.4)	7.3(0.6)	6	0.15	8.4	
4.03	+0.02	0.47(0.02)	25.7(1.5)	11.0(0.6)	8	0.15	11.0	t
4.17	−0.03	0.47(0.02)	37.9(2.4)	8.6(0.9)	8	0.14	9.2	
4.26	+0.02	0.45(0.03)	24.4(1.7)	11.9(0.7)	8	0.11	12.2	
4.49	+0.02	0.55(0.04)	15.5(1.1)	9.1(0.5)	6	0.11	11.6	
4.64	−0.03	0.45(0.02)	26.6(1.6)	8.4(0.7)	8	0.11	9.6	
4.72	+0.02	0.62(0.02)	49.0(1.6)	1.8(0.7)	8	0.12	11.5	
4.87	−0.03	0.72(0.04)	28.4(1.7)	8.0(0.7)	5	0.17	8.3	
4.95	+0.02	0.49(0.02)	29.1(1.7)	12.4(0.7)	8	0.13	8.5	
5.10	−0.03	0.54(0.02)	48.2(2.3)	10.6(1.0)	6	0.16	8.5	
5.19	+0.02	0.81(0.02)	35.1(1.1)	9.4(0.5)	6	0.11	9.0	
5.33	−0.03	0.61(0.02)	24.4(1.0)	12.2(0.4)	8	0.10	10.2	
5.42	+0.02	0.59(0.04)	20.3(1.4)	12.1(0.6)	5	0.14	10.6	
5.56	−0.03	0.59(0.03)	44.5(2.3)	8.9(0.9)	8	0.14	10.0	
5.65	+0.02	0.69(0.03)	23.2(1.0)	11.2(0.4)	8	0.10	12.3	
			Field 2d					
5.80	−0.03	0.75(0.04)	22.8(1.3)	10.3(0.6)	6	0.16	7.4	
5.88	+0.02	0.85(0.03)	30.9(1.1)	10.6(0.5)	8	0.13	8.6	
6.02	−0.02	0.75(0.04)	25.0(1.5)	13.1(0.6)	8	0.16	4.2	
6.11	+0.03	0.89(0.06)	9.6(0.8)	23.4(0.3)	6	0.18	4.2	
6.25	−0.02	0.70(0.03)	30.8(1.8)	16.4(0.7)	6	0.16	5.6	
6.34	+0.03	0.86(0.05)	29.4(1.9)	16.3(0.8)	5	0.22	5.6	
6.48	−0.02	0.79(0.03)	29.0(1.3)	15.1(0.6)	8	0.15	8.0	
6.57	+0.03	1.11(0.06)	8.4(0.6)	6.6(0.2)	3	0.22	6.8	t
6.72	−0.02	1.02(0.03)	24.1(0.9)	14.5(0.4)	5	0.14	10.0	
6.80	+0.03	0.94(0.02)	28.0(0.9)	15.4(0.4)	5	0.12	11.4	

Table 6.1: *Continued*

l (^{o})	b (^{o})	T_L/T_{sys} $\times 10^3$	ΔV (km s^{-1})	$V_{\rm LSR}$ (km s^{-1})	V_{res} (km s^{-1})	RMS[1] $\times 10^3$	t_{int} (hrs)	Note
Field 3 (G13.9+0.0)								
13.04	−0.46	0.77(0.03)	31.8(1.2)	26.0(0.5)	8	0.13	7.9	
13.13	−0.41	0.41(0.02)	43.3(3.0)	28.7(1.2)	8	0.13	10.6	
13.22	−0.36	0.61(0.03)	39.5(2.5)	26.0(1.1)	6	0.17	8.2	
13.30	−0.36				6	0.18	8.4	
13.39	−0.26	0.80(0.03)	39.4(1.7)	27.4(0.7)	8	0.14	8.4	
13.48	−0.22	0.76(0.01)	34.3(0.8)	24.9(0.3)	6	0.12	11.2	
13.57	−0.17	1.01(0.03)	40.9(1.4)	29.2(0.6)	5	0.16	9.3	
13.65	−0.12	0.85(0.03)	32.5(1.3)	26.9(0.6)	6	0.14	9.1	
13.74	−0.07	0.90(0.03)	31.5(1.3)	25.9(0.5)	8	0.18	8.0	
13.83	−0.02	1.00(0.03)	38.3(1.5)	30.4(0.6)	5	0.21	8.8	
13.92	+0.03	1.15(0.03)	48.4(1.4)	33.4(0.6)	8	0.19	6.3	
14.00	+0.07	1.10(0.03)	27.1(0.8)	26.2(0.3)	6	0.17	6.7	
14.09	+0.12	0.94(0.03)	30.3(1.1)	24.7(0.5)	5	0.15	10.0	
14.18	+0.17	0.83(0.02)	40.2(1.4)	24.5(0.6)	6	0.13	10.9	
14.27	+0.22	0.80(0.02)	36.6(1.0)	30.4(0.4)	8	0.13	9.9	
14.36	+0.26	0.82(0.02)	38.4(1.4)	30.0(0.6)	5	0.13	11.7	
14.44	+0.31	0.68(0.03)	26.3(1.4)	25.1(0.6)	8	0.14	7.5	
14.53	+0.36	0.63(0.02)	34.9(1.3)	29.8(0.5)	8	0.13	8.0	
14.62	+0.41	0.63(0.02)	34.8(1.4)	28.6(0.6)	8	0.14	10.1	
14.71	+0.46	0.76(0.03)	22.6(0.9)	25.0(0.4)	6	0.11	11.8	
Field 4 (G25.2+0.0)								
24.37	−0.44				8	0.13	10.2	
24.46	−0.39	0.46(0.03)	19.1(1.3)	104.3(0.5)	8	0.10	10.6	
24.55	−0.35				8	0.16	8.4	
24.64	−0.30				8	0.14	9.3	
24.73	−0.25	0.47(0.03)	37.0(2.6)	107.2(1.0)	8	0.17	10.4	t
24.81	−0.21				8	0.16	8.3	
24.90	−0.16	0.33(0.02)	61.1(4.7)	95.3(1.6)	8	0.13	14.3	
24.99	−0.12				8	0.10	13.9	
25.08	−0.07				8	0.15	8.4	
25.17	−0.02				5	0.16	10.2	
25.26	+0.03				8	0.13	12.4	
25.35	+0.07				8	0.12	13.2	
25.43	+0.12				8	0.14	10.7	
25.52	+0.16				8	0.13	10.9	
25.61	+0.21				8	0.13	9.5	
25.70	+0.26				8	0.15	9.5	
25.79	+0.30	0.55(0.02)	38.6(1.6)	110.6(0.7)	8	0.14	7.2	
25.88	+0.35	0.56(0.02)	23.3(0.8)	102.1(0.4)	8	0.12	9.7	
25.96	+0.40	0.57(0.03)	16.0(0.9)	99.4(0.4)	8	0.11	8.2	
26.05	+0.44	0.47(0.03)	22.2(1.9)	103.2(0.8)	8	0.13	10.6	

Table 6.1: *Continued*

l (^{o})	b (^{o})	T_L/T_{sys} $\times 10^3$	ΔV (km s^{-1})	$V_{\rm LSR}$ (km s^{-1})	V_{res} (km s^{-1})	RMS[1] $\times 10^3$	t_{int} (hrs)	Note
Field 5 (G27.5+0.0)								
26.62	−0.43	0.63(0.01)	33.1(0.8)	95.9(0.3)	8	0.13	7.1	
26.71	−0.39	0.35(0.03)	40.4(3.7)	90.4(1.5)	8	0.13	9.6	
26.80	−0.34	0.45(0.02)	37.2(1.7)	100.3(0.7)	8	0.11	7.6	
26.88	−0.30	0.40(0.03)	49.9(4.9)	101.4(1.7)	8	0.13	10.3	
26.97	−0.25	0.61(0.03)	46.3(2.4)	90.3(1.0)	8	0.17	5.5	
27.06	−0.20	0.68(0.03)	42.7(2.3)	92.8(1.0)	8	0.16	8.0	
27.15	−0.16	0.38(0.02)	23.0(1.4)	88.4(0.6)	8	0.11	8.6	
27.24	−0.11	0.60(0.02)	21.1(0.8)	95.0(0.4)	8	0.11	11.5	
27.33	−0.06	0.53(0.02)	24.1(1.2)	94.5(0.5)	8	0.13	8.9	
27.42	−0.02	0.52(0.03)	24.2(1.5)	90.8(0.6)	8	0.13	10.0	
27.50	+0.03	0.59(0.05)	15.4(1.4)	94.5(0.6)	8	0.15	8.3	
27.59	+0.07	0.61(0.04)	21.1(1.4)	94.5(0.6)	8	0.13	10.2	
27.68	+0.12	0.50(0.03)	16.3(1.2)	88.9(0.5)	8	0.13	8.5	t
27.77	+0.16	0.31(0.02)	33.0(2.9)	92.8(1.2)	8	0.10	10.1	
27.86	+0.21	0.35(0.02)	39.8(3.1)	88.9(1.2)	8	0.17	6.8	
27.95	+0.26	0.65(0.02)	29.8(1.1)	85.0(0.5)	8	0.10	8.2	
28.04	+0.31	0.53(0.02)	34.8(1.9)	92.1(0.8)	5	0.14	15.0	
28.13	+0.35	0.41(0.02)	31.1(1.4)	89.3(0.6)	8	0.08	18.6	
28.21	+0.40	0.45(0.02)	48.7(2.9)	91.7(1.0)	8	0.14	7.6	
28.30	+0.44	0.53(0.03)	24.2(1.8)	100.3(0.7)	8	0.14	9.2	
Field 6a (G34.2+0.0)								
33.05	−0.02				8	0.13	12.4	
33.14	+0.03				8	0.16	12.4	
33.28	−0.02				8	0.14	11.1	
33.37	+0.03				8	0.12	14.1	
33.50	−0.02				8	0.13	15.2	
33.59	+0.03				8	0.13	18.6	
33.73	−0.02				8	0.13	10.8	
33.82	+0.03				8	0.12	13.0	
33.95	−0.02				8	0.16	10.6	
34.04	+0.03				8	0.15	9.4	
34.18	−0.02				5	0.18	9.7	
34.27	+0.03	0.38(0.03)	16.8(1.4)	47.4(0.6)	8	0.10	13.1	
34.40	−0.02				8	0.19	9.0	
34.49	+0.03				8	0.14	12.2	
34.63	−0.02				8	0.14	9.8	
34.72	+0.03				8	0.10	13.3	
34.85	−0.02				8	0.14	8.9	
34.94	+0.03	0.35(0.02)	39.0(2.5)	56.5(1.0)	8	0.12	11.0	
35.08	−0.02	0.30(0.02)	38.6(3.0)	52.4(1.2)	8	0.10	8.9	
35.17	+0.03				8	0.20	11.9	

Table 6.1: *Continued*

l (^{o})	b (^{o})	T_L/T_{sys} $\times 10^3$	ΔV (km s^{-1})	$V_{\rm LSR}$ (km s^{-1})	V_{res} (km s^{-1})	RMS[1] $\times 10^3$	t_{int} (hrs)	Note
Field 6b (G36.5+0.0)								
35.31	−0.02	0.32(0.02)	45.4(3.4)	54.2(1.4)	8	0.11	11.1	
35.40	+0.03	0.36(0.02)	45.1(2.3)	57.5(1.0)	8	0.10	14.3	
35.53	−0.02	0.56(0.02)	36.7(1.6)	55.9(0.7)	8	0.16	7.2	
35.62	+0.03				8	0.13	9.4	
35.76	−0.02	0.21(0.02)	31.6(3.8)	60.5(1.5)	6	0.10	10.7	t
35.85	+0.02				8	0.13	13.0	
35.98	−0.02				8	0.13	11.7	
36.07	+0.03				5	0.13	13.0	
36.21	−0.02				8	0.12	10.6	
36.30	+0.02				8	0.16	13.8	
36.43	−0.02	0.61(0.03)	21.2(1.5)	82.0(0.6)	8	0.13	10.9	
		0.46(0.03)	25.3(2.3)	47.5(0.89)	8	0.13	10.9	
36.52	+0.02	0.27(0.02)	47.1(3.8)	71.9(1.5)	8	0.11	9.0	
36.66	−0.02	0.43(0.03)	26.1(2.1)	79.3(0.9)	8	0.11	10.8	
36.75	+0.02				8	0.12	13.0	
36.89	−0.02				8	0.15	9.9	
37.11	−0.02				8	0.17	12.2	
37.20	+0.03	0.29(0.02)	46.2(3.4)	69.8(1.3)	8	0.11	14.2	
37.34	−0.02	0.48(0.03)	31.5(2.2)	73.8(0.9)	8	0.17	5.4	
37.43	+0.02				8	0.15	9.9	
Field 6c (G38.7+0.0)								
37.56	−0.02				8	0.14	12.0	
37.65	+0.02				8	0.15	15.5	
37.79	−0.02				8	0.15	14.4	
37.88	+0.02				8	0.17	8.4	
38.01	−0.02	0.46(0.03)	46.7(3.3)	59.8(1.4)	8	0.14	9.3	
38.10	+0.02				8	0.14	14.0	
38.24	−0.03	0.33(0.02)	51.6(3.5)	58.6(1.4)	8	0.12	8.6	
38.33	+0.02				8	0.16	9.1	
38.46	−0.03	0.50(0.03)	21.5(1.6)	40.0(0.7)	8	0.13	9.7	
38.55	+0.02				8	0.13	12.5	
38.69	−0.03				8	0.19	6.8	
38.78	+0.02				8	0.14	9.1	
38.91	−0.03				8	0.15	10.9	
39.00	+0.02				8	0.11	12.3	
39.14	−0.02				8	0.26	2.6	
39.22	+0.03				8	0.21	4.9	
39.36	−0.02				8	0.20	4.3	
39.45	+0.03				8	0.19	5.9	
39.59	−0.02				8	0.18	4.2	
39.68	+0.03				8	0.16	6.6	

Table 6.1: *Continued*

l (^{o})	b (^{o})	T_L/T_{sys} $\times 10^3$	ΔV (km s^{-1})	$V_{\rm LSR}$ (km s^{-1})	V_{res} (km s^{-1})	RMS[1] $\times 10^3$	t_{int} (hrs)	Note
			Field 7 (G45.5+0.0)					
44.67	−0.44	0.30(0.03)	28.3(2.9)	56.1(1.2)	8	0.12	9.0	t
44.76	−0.40				8	0.14	9.5	t
44.85	−0.35				8	0.12	10.4	
44.94	−0.30				8	0.12	9.2	
45.03	−0.25				8	0.13	10.5	
45.12	−0.21				8	0.10	13.8	
45.20	−0.16				8	0.10	10.3	
45.29	−0.11				8	0.11	12.0	
45.38	−0.07				8	0.10	10.5	
45.47	−0.02	0.42(0.02)	11.2(0.7)	55.1(0.3)	8	0.10	14.6	t
45.56	+0.03	0.38(0.02)	36.2(2.4)	44.9(1.0)	8	0.13	9.8	
45.64	+0.08				8	0.12	15.1	
45.73	+0.12				8	0.19	6.3	
45.82	+0.17				8	0.14	11.0	
45.91	+0.22				8	0.13	10.2	
46.00	+0.26				8	0.16	10.3	
46.08	+0.31				8	0.14	9.6	
46.17	+0.36				8	0.11	9.7	
46.26	+0.41	0.53(0.04)	16.0(1.3)	43.9(0.5)	8	0.10	9.5	
		0.28(0.04)	17.0(2.5)	12.8(1.0)	8	0.10	9.5	
46.35	+0.45				8	0.12	11.7	
			Field 8 (G56.9+0.0)					
56.08	−0.46	0.47(0.03)	32.7(2.7)	23.0(1.1)	8	0.13	12.8	
56.17	−0.42	0.24(0.02)	30.6(3.5)	24.5(1.4)	8	0.10	13.7	
56.26	−0.37	0.35(0.03)	54.8(6.8)	37.0(2.5)	8	0.15	9.9	
56.34	−0.32				8	0.14	12.7	
56.43	−0.27	0.33(0.03)	25.2(2.8)	31.3(1.1)	8	0.13	12.5	t
56.52	−0.22				8	0.09	16.1	
56.60	−0.17	0.37(0.02)	37.3(3.4)	24.3(1.2)	8	0.13	8.2	
56.69	−0.12				8	0.13	12.4	
56.78	−0.07	0.47(0.03)	27.6(2.4)	23.8(1.0)	8	0.14	10.1	
56.86	−0.02				8	0.15	13.2	
56.95	+0.03	0.21(0.01)	32.4(2.5)	25.3(1.0)	8	0.08	13.1	t
57.04	+0.08	0.21(0.02)	49.5(7.0)	13.5(2.4)	8	0.10	16.8	
57.12	+0.13	0.22(0.02)	64.3(11.2)	15.0(3.1)	8	0.11	11.1	
57.21	+0.18				8	0.16	15.1	
57.30	+0.23	0.39(0.02)	29.0(1.7)	12.5(0.6)	8	0.12	8.6	
57.38	+0.28				8	0.10	11.6	
57.47	+0.33				8	0.16	9.5	
57.56	+0.38	0.27(0.02)	44.4(3.1)	17.2(1.3)	8	0.12	12.0	
57.65	+0.42	0.30(0.02)	51.7(3.7)	19.7(1.4)	8	0.13	9.5	
57.73	+0.47				8	0.15	11.4	

Table 6.1: *Continued*

l (°)	b (°)	T_L/T_{sys} $\times 10^3$	ΔV (km s^{-1})	$V_{\rm LSR}$ (km s^{-1})	V_{res} (km s^{-1})	RMS[1] $\times 10^3$	t_{int} (hrs)	Note
Field 9 (G66.2+0.0)								
65.39	−0.50	0.38(0.02)	44.7(2.8)	13.0(1.2)	8	0.10	11.6	
65.48	−0.45	0.44(0.03)	37.5(3.1)	5.4(1.3)	8	0.13	12.1	
65.56	−0.39	0.33(0.03)	44.7(4.4)	4.8(1.5)	8	0.13	8.9	
65.65	−0.34				8	0.12	9.6	
65.73	−0.29				8	0.15	5.8	
65.82	−0.24				8	0.14	10.8	
65.90	−0.18				8	0.13	12.1	
65.99	−0.13				8	0.08	17.3	
66.08	−0.08				8	0.16	4.8	
66.16	−0.03				8	0.16	4.1	
66.24	+0.03	0.67(0.02)	43.9(1.6)	14.9(0.7)	8	0.14	8.8	
66.33	+0.08	0.42(0.04)	44.3(4.5)	3.2(1.8)	8	0.15	11.1	
66.41	+0.13				8	0.22	7.5	
66.50	+0.19				8	0.19	8.4	
66.59	+0.24				8	0.13	11.5	
66.67	+0.29				8	0.11	13.8	
66.75	+0.35	0.33(0.03)	38.2(4.2)	10.2(1.8)	8	0.15	7.7	t
66.84	+0.40	0.27(0.02)	42.6(3.4)	8.3(1.4)	8	0.11	12.2	t
66.92	+0.45				8	0.16	8.5	
67.01	+0.50				8	0.14	9.4	

1) RMS is in units of T_L/T_{sys}.
Note: t – tentative detection.

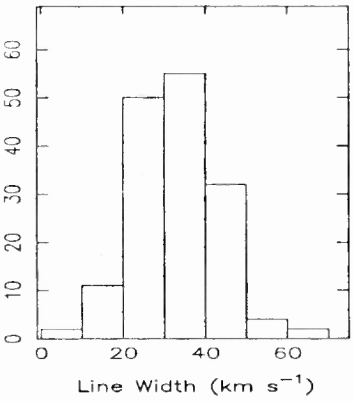

Figure 6.1: Histogram of the width of the hydrogen lines detected in the observations with a resolution of 2° × 6′.

G347.70−0.20 differ by more than a factor of 2. These two positions are separated in declination by only 0°.1. The range in the central velocity of the lines observed towards fields with $l < 35°$ is typically 15 km s^{-1} . This difference is about half the typical line width observed in the survey. RRLs are not detected in many positions within the fields with $l > 35°$.

6.3 Line Widths

Width of the lines detected in the 2° × 6′ observations are in the range 20 – 45 km s^{-1} . Fig. 6.1 shows the histogram of the observed line widths. The median line width is 32.5 km s^{-1} . This width is marginally large compared to the width of lines from normal H II regions ($\sim$ 26 km s^{-1} ; Lockman et al. 1996). Line widths near 327 MHz can be affected by pressure broadening (see Section 5.1) and blending of lines from objects within the beam area or from objects along the line of sight with different central velocities. The estimated densities of the line emitting region (see Section 5.4) are not high enough for pressure broadening to be significant. Thus the relatively larger line widths are probably due to blending of lines from different objects along the line-of-sight and over the beam. In a couple of positions, the line width observed is less than 10 km s^{-1} , which constrains the kinematic temperature of the line emitting region to < 2200 K.

Comparison of the distribution of line widths obtained from the observations with 2° × 2° (see Section 3.3.1) and 2° × 6′ beams shows that they are similar. The median widths from the low resolution observations is $\sim$ 31 km s^{-1} . As discussed above the width of the observed lines is not affected by pressure broadening but most likely due to blending of lines from different objects either along the line of sight or within the beam. Since the number of line emitting zones inside the 2° × 2° beam can be larger than that inside the high resolution beam, we may expect larger widths in the low resolution

survey. But the low resolution observations are not sensitive to line emitting zones of relatively small angular extent due to beam dilution. On the other hand, such line emitting zones can contribute to line emission observed with the $2^\circ \times 6'$ beam. Thus it is possible for the lines detected in the two observations to have similar median widths. Examination of the distribution of the widths, obtained from the two observations, shows that lines with width between 50 – 70 km s^{-1} are observed more frequently in the low resolution survey. These large widths are most likely due to blending of lines from different objects within the coarse beam. Towards a few positions, line with widths ~ 10 km s^{-1} has been observed in the high resolution survey. Such narrow lines are not detected in any of the positions in the $2^\circ \times 2^\circ$ observations.

6.4 *lv* Diagram

The *lv* diagram obtained from the high resolution observations is shown in Fig. 6.2. The central velocities and the width of the lines detected towards the 9 fields are marked along with the *lv* curves corresponding to (a) the four spiral arms (1 to 4 as designated by Taylor & Cordes 1993), (b) galactocentric radii of 3.5 (dashed line) and 7 kpc (dotted line) and (c) the terminal velocity at different galactic longitudes (dash-dot-dot-dot line; see Section 4.1 for details). The *lv* diagram shows some confinement of line emission to the spiral arms 2 and 3 below $l = 50^\circ$. At longitudes $l > 50^\circ$ the line emission does not seem to be confined to any of the spiral arms.

Similarities are seen in the *lv* diagram shown in Fig. 6.2 with that obtained by Anantharamaiah (1985a) from the H272α line observations with a beam of $2^\circ \times 6'$. In his observations, H272α lines were observed towards a selected set of sources in the longitude range $-2^\circ < l < 50^\circ$. The concentration of line emission towards Galactocentric radius of ~ 5.0 kpc near longitude 15° and the extension of emission to negative velocities in the longitude range $l < 10^\circ$ are evident in both the *lv* diagrams. However, lines with width > 70 km s^{-1} which were observed by Anantharamaiah (1985a) are not seen in the present survey.

The *lv* diagram obtained from the observations with a $2^\circ \times 6'$ beam shows, in general, good similarity with that obtained from the low resolution survey (see Section 4.1). In field 7 (G45.5+0.0) a line feature with central velocity 12 km s^{-1} is detected towards G46.26+0.41. This feature falls within the *lv* space marked as "no line emission region" in the *lv* diagram (Fig. 4.1) obtained from the low resolution survey data (see Section 4.1). Examination of the spectra towards G45.5+0.0 observed with the $2^\circ \times 2^\circ$ beam (see Fig 3.1a) shows the presence of a possible weak feature corresponding to this emission line. The line emission observed in the high resolution survey at longitude $l > 50^\circ$ shows extension towards the negative velocities in the *lv* space which is not observed in the low resolution survey.

6.5 Comparison with the Low Resolution Observations

We have made observations with the $2^\circ \times 6'$ beam towards seven fields which are 2° wide and two fields which are 6° wide. The low resolution survey had detected lines in all these fields. With the higher resolution beam, 20 independent positions can be observed

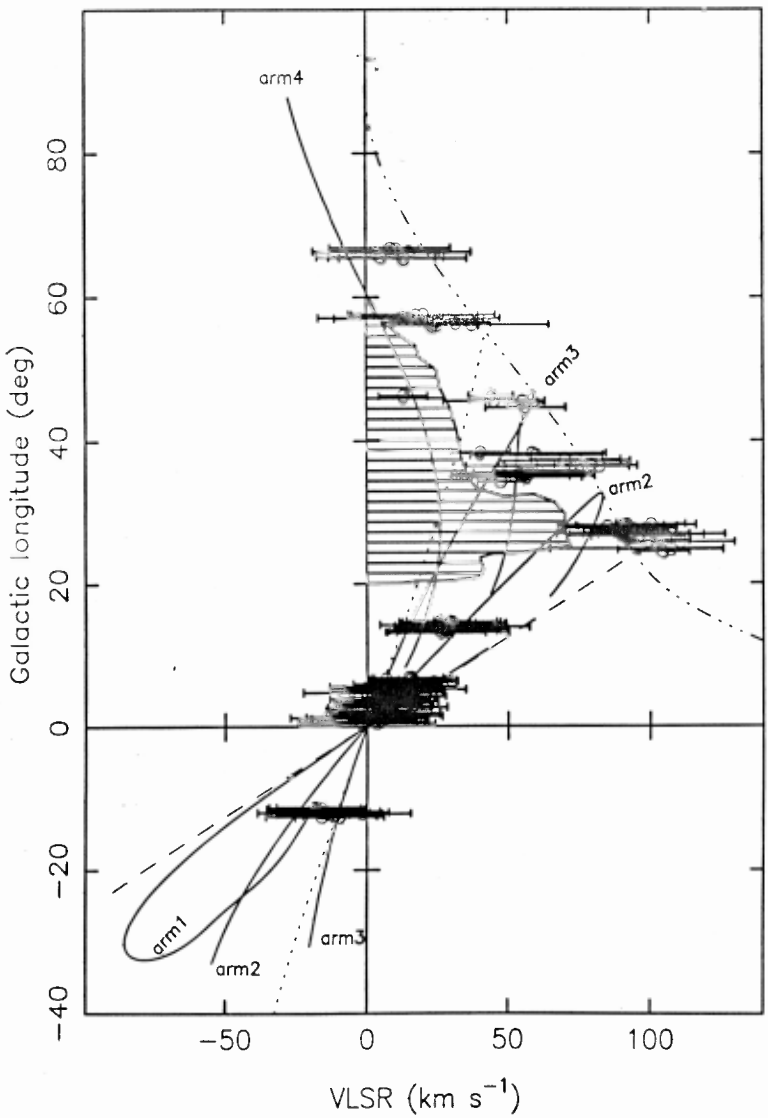

Figure 6.2: *lv* diagram obtained from the hydrogen line emission observed with the $2^\circ \times 6'$ beam. The open circles represent the central velocity and the horizontal lines indicates the line width. The delineations correspond to the four spiral arms (1 to 4 as designated by Taylor & Cordes 1993), the *lv* diagram corresponding to an annulus of 3.5 kpc (dashed line) and 7 kpc (dotted line) and the terminal velocity at different galactic longitude (dash-dot-dot-dot line).

within the $2^\circ \times 2^\circ$ beam of the lower resolution survey. The positions observed at higher resolution are therefore segregated into sets of 20 samples. Our aim is to average the 20 spectra in each of these sets and compare it with the spectrum obtained with the low resolution beam in the same direction and also to examine all the spectra within a 2° field for possible variations.

We show below that the average spectrum, obtained from the the 20 adjacent high resolution beam observations, is equivalent to the spectrum observed in the low resolution survey towards the same direction. The SNR of the two spectra will differ by the square root of the ratio of the total integration times involved. This is strictly true only if the data obtained with the higher resolution beam is weighted in a similar fashion as the angular response of the lower resolution beam. In the following discussion we assume that this is true. Consider two sets of observations with beam Ω_1 and Ω_2, where $\Omega_1 > \Omega_2$. Our aim is to compare the SNR of the spectrum obtained with the beam Ω_1 with that obtained by averaging the spectra observed with the beams Ω_2. Let Ω_1 be completely covered with n Ω_2 beams and let the line emission be present only at m positions ($m < n$). For simplicity, we assume that there is no beam dilution for the m positions when observed with the beam Ω_2. Let each of the n position be observed for a time τ_2 and the integration time of the observation with the beam Ω_1 be τ_1. We also assume, for simplicity, that the sky background temperature is uniform over Ω_1 and the receiver temperatures of the two telescopes are the same. The noise in the spectrum obtained with the beam Ω_1 is

$$\Delta T_{rms} = \frac{K T_{sys}}{\sqrt{\beta \tau_1}}, \tag{6.1}$$

where ΔT_{rms} is the R.M.S noise in temperature units, K is a factor which depends on the method used for measuring the spectrum, T_{sys} is the system temperature, which is the sum of the sky temperature and the receiver temperature and β is the spectral resolution. The line antenna temperature T_{LA} is given by

$$T_{LA} = T_L \frac{m\Omega_2}{\Omega_1} \tag{6.2}$$

where T_L is the line brightness temperature, which is multiplied by the beam dilution factor to get the antenna temperature. We have also assumed that T_L is same for the m emission zones. The SNR is then given by

$$SNR = \frac{T_L}{K T_{sys}} \sqrt{\beta \tau_1} \frac{m\Omega_2}{\Omega_1} \tag{6.3}$$

The R.M.S noise, the line antenna temperature and the SNR of the spectrum obtained by averaging n spectra observed with the beam Ω_2 are

$$\Delta T'_{rms} = \frac{1}{\sqrt{n}} \frac{K T_{sys}}{\sqrt{\beta \tau_2}} \tag{6.4}$$

$$T'_{LA} = \frac{m}{n} T_L \tag{6.5}$$

$$SNR' = \frac{T_L}{K T_{sys}} \sqrt{\beta n \tau_2} \frac{m}{n} \tag{6.6}$$

Considering the fact that $\Omega_1/\Omega_2 = n$, the SNRs differ only by the factor $\sqrt{\frac{\tau_1}{n\tau_2}}$.

There are several effects which can make the average spectrum different from the spectrum obtained in the low resolution survey in the same direction. Some of them are listed below.

1. The 20 spectra are averaged without taking into account of the angular response function of the low resolution beam.

2. Some of the assumptions made in deriving the SNRs in the above analysis, for example, equal integration time at different positions in the high resolution observation and uniform system temperature at different positions within the low resolution beam, are not true in practice. Both these effects can make the average spectrum different from that obtained in the low resolution survey. The averaging of the 20 spectra takes into account the channel weights, which are proportional to the integration time per channel. Thus the spectra with larger integration time will have higher weight. The observed spectra are normalized with the system temperature and the average of these spectra are used for comparison. The normalization is equivalent to weighting with the inverse of the system temperature and thus is not identical to the average of the unnormalized spectra if there are large changes in the system temperature from position to position. Because of lack of a better strategy, we have used the normalized spectra for the present work.

3. The beam centers of the 20 positions observed in the full telescope survey towards a $2^\circ \times 2^\circ$ area are placed along the theoretical major axis of the elliptic beam of the low resolution survey. Since the actual beam shape depends on the phasing of the telescope (see Section 2.2), it is not known whether the theoretical major axis and the major axis of the telescope response matches well. Also, in a few cases, the 20 beam centers are positioned along the galactic plane. Thus the "effective" beam obtained when the 20 spectra are averaged will not be identical to the sky area sampled in the low-resolution observations.

The spectrum obtained by averaging the 20 spectra towards a given $2^\circ \times 2^\circ$ region and that observed in the same direction in the low resolution survey are shown in Fig. 6.5 to 6.18. Table 6.2 gives the line parameters (columns 3,4,5) obtained from these spectra along with the spectral resolution (column 6) and the effective integration time (column 8). The note "AVG" and "Module" given in column 9 indicate the average spectrum and the spectrum obtained in the low resolution survey respectively. Examination of Table 6.2 shows that the parameters of the hydrogen line in the average spectrum in most of the fields agree, within the signal to noise ratio, with those of the spectrum obtained in the low resolution survey towards the same direction. In fields 1 and 8, the line width observed in the low resolution survey and that obtained from the average spectrum are different. The line emission appears to be complex in the field 6c, which makes it difficult to fit a proper baseline to the spectrum. A larger bandwidth is required for observation in this direction, since line emission seems to extend over a large velocity range.

Two fields where the line structure in the average spectrum is different from that of the corresponding spectrum from the low resolution survey are fields 6a and 9 (Figs. 6.13 & 6.18). The average spectrum towards field 6a consists of two hydrogen line features. The line feature with central velocity close to that observed in the low resolution survey has line width 27.9 km s^{-1} which is larger than the width of the line (14.2 km s^{-1}) observed with a $2^\circ \times 2^\circ$ beam. If we assume that the line intensities (in units of T_L/T_{sys}) in the average spectrum and the spectrum obtained with the $2^\circ \times 2^\circ$ beam are similar, then the line features seen in the average spectrum should be at about the

Table 6.2: Line parameters from the low resolution observation and the average spectrum

Field Name	$l(b=0^o)$ (^{o})	T_L/T_{sys} $\times 10^3$	ΔV (km s^{-1})	$V_{\rm LSR}$ (km s^{-1})	V_{res} (km s^{-1})	RMS[1] $\times 10^3$	t_{int} (hrs)	Note
Field 1	348.0	0.51(0.02)	35.9(1.5)	−15.5(0.6)	2	0.08	214.1	AVG
	348.0	0.42(0.02)	53.6(2.9)	−22.6(1.2)	8	0.12	12.7	Module
Field 2b	2.3	0.43(0.01)	29.2(1.1)	5.1(0.5)	2	0.06	207.9	AVG
	2.3	0.37(0.02)	26.0(2.0)	10.2(0.8)	8	0.10	10.7	Module
Field 2c	4.7	0.56(0.01)	34.3(1.0)	8.6(0.4)	2	0.06	199.5	AVG
	4.7	0.67(0.02)	28.7(0.9)	11.3(0.4)	8	0.09	13.2	Module
Field 3	13.9	0.76(0.02)	34.9(0.8)	27.5(0.3)	2	0.07	182.9	AVG
	13.9	0.90(0.02)	37.7(0.7)	26.7(0.3)	8	0.08	16.8	Module
Field 4	25.2	0.28(0.01)	30.0(1.7)	101.8(0.7)	3	0.06	205.8	AVG
	25.2	0.44(0.01)	25.5(0.8)	98.2(0.4)	6	0.10	19.8	Module
Field 5	27.5	0.43(0.01)	31.9(1.0)	92.7(0.4)	3	0.05	189.7	AVG
	27.5	0.39(0.02)	28.5(1.4)	91.6(0.6)	8	0.08	18.2	Module
Field 6a	34.2	0.15(0.02)	15.2(1.8)	90.4(0.8)	3	0.05	235.2	AVG
		0.17(0.01)	27.9(2.2)	50.8(0.9)	3	0.05	235.2	AVG
	34.2	0.26(0.02)	14.2(0.9)	45.6(0.4)	5	0.08	38.4	Module
Field 6b	36.5	0.27(0.01)	55.6(2.4)	64.7(1.0)	5	0.06	209.1	AVG
	36.5	0.25(0.01)	60.0(3.2)	65.2(1.2)	8	0.07	33.5	Module
Field 6c	38.7				3	0.09	181.1	AVG
	38.7				8	0.07	27.6	Module
Field 7	45.5	0.18(0.01)	44.6(2.6)	47.5(1.1)	3	0.05	213.0	AVG
	45.5	0.20(0.01)	40.5(2.2)	48.8(0.9)	8	0.05	53.5	Module
Field 8	56.9	0.24(0.01)	48.0(2.1)	21.2(0.9)	5	0.05	240.3	AVG
	56.9	0.25(0.01)	21.2(1.6)	20.9(0.7)	8	0.06	46.2	Module
Field 9	66.2	0.25(0.01)	49.1(1.7)	9.9(0.7)	5	0.04	196.0	AVG
	66.2				8	0.07	45.2	Module

1) RMS is in units of T_L/T_{sys}

2σ level in the spectrum obtained in the low resolution survey towards field 6a. Towards field 9, no line emission is detected in the low resolution survey whereas a line feature is detected (see Table 6.2) in the average spectrum. The line feature seen in the average spectrum should have been at $> 3\sigma$ level in the spectrum obtained in the low resolution survey if we assume that the line intensities in both spectra are similar. While the observations towards field 6a may be consistent within the signal to noise ratio, further investigation is required to understand the discrepancy observed towards field 9.

6.6 Angular Extent of the Line Emitting Region

In this section we will try to answer the question "Are the line emitting zones constituted of ionized clumps with emission confined to small angular regions or is the emission extended and uniform over a large area ? " The higher resolution observations show different behavior of line emission for $l < 35°$ and for $l > 35°$. While RRLs were detected in almost all the individual positions within the fields with $l < 35°$, lines were not detected in several individual positions within the fields in the longitude range $l = 35°$ to $85°$.

If the line emission originates from a homogeneous, ionized region with angular extent of several degrees, then the line parameters observed at positions within this angular span are expected to be similar. Examination of the observed spectra at different fields with $l < 35°$ shows that at several positions there is a considerable change in the line parameters when the beam centre is moved by even $6'$ in declination. For example, towards the position G4.72+0.02, the detected line has a width of 49 km s^{-1} and a central velocity of 1.8 km s^{-1} while the line parameters at G4.64−0.03 are ΔV = 27 km s^{-1} and V_{LSR} = 8.4 km s^{-1} . The beam centers of these two positions differ by 0°.1. This difference implies that the line emitting zones have structures on an angular scale of $\sim 0°.1$, which is $\sim$ 10 pc, if the distance to the source producing the line emission is 5 kpc. This scale is smaller than the typical size of the line emitting regions estimated in section 5.4. We therefore conclude that the line emission in fields with $l < 35°$ originate from ionized regions extending over several degrees which may have clumps with angular structures as small as 0°.1.

As mentioned earlier the lines are not detected at many individual positions in fields beyond $l = 35°$. Here we present the analysis towards one of the fields – G45.5+0.0.

6.6.1 Line emission towards the Field G45.5+0.0

The line of sight over an angle of 2° towards G45.5+0.0 through the galactic disk is shown in Fig. 6.3. The line-of-sight intersects the spiral arm 4 at one position and arm 3 at two places. The distances to the three regions of intersection are $\sim$ 4.7 kpc, 7.8 kpc and 10.7 kpc. The expected radial velocities for these distances are 58, 56 and 17 km s^{-1} respectively. H II regions identified from higher frequency RRL observations in this field are listed in Table 6.3 along with the line parameters. RRL near 327 MHz is detected towards some of these positions and their parameters are also given in Table 6.3. The central velocity of 327 MHz lines and that detected from H II regions are comparable.

Examination of the 20 spectra obtained from field 7 (Fig. 6.16) shows unambiguous presence of lines in only 3 positions. If the line emission is confined to only these 3 positions, then the expected SNR of the spectrum obtained by averaging 20 spectra is

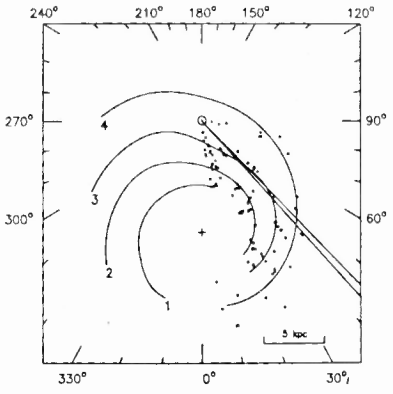

Figure 6.3: The line of sight through the galactic disk at $l = 45°.5$. The four spiral arms (curved solid lines) and the H II regions (dots) with known distances in the first quadrant are also marked.

Table 6.3: H II regions and RRLs near 327 MHz in field 7 (G45.5+0.0)

l	b	T_L	ΔV	$V_{\rm LSR}$	λ_{obs}	Note
(^{o})	(^{o})	(mK)	(km s^{-1})	(km s^{-1})	(cm)	
44.786	−0.490	17(2.5)	30.0(5.5)	44.8(4.0)	9	L89
44.981	−0.646	14(2.0)	20.3(3.4)	67.3(1.4)	9	lph96
45.125	0.136	67(4.9)	31.6(2.7)	57.6(1.1)	3	L89
45.451	0.060	153(6.3)	27.9(1.3)	55.9(0.6)	3	L89
45.475	0.130	57(3.9)	27.5(2.1)	56.0(0.9)	3	L89
45.824	−0.290	16(2.0)	38.7(5.8)	62.3(4.2)	3	L89
46.495	−0.247	83(5.1)	22.4(1.6)	57.2(0.7)	3	L89
RRLs near 327 MHz in field 7						
l	b	T_L/T_{sys}	ΔV	$V_{\rm LSR}$		Note
(^{o})	(^{o})		(km s^{-1})	(km s^{-1})		
44.67	−0.44	0.30(0.03)	28.3(2.9)	56.1(1.2)		t
45.47	−0.02	0.42(0.02)	11.2(0.7)	55.1(0.3)		t
45.56	+0.03	0.38(0.02)	36.2(2.4)	44.9(1.0)		
46.26	+0.41	0.53(0.04)	16.0(1.3)	43.9(0.5)		
		0.28(0.04)	17.0(2.5)	12.8(1.0)		

Note: L89 – Lockman (1989); lph96 – Lockman et al. (1996);
t – tentative detection.

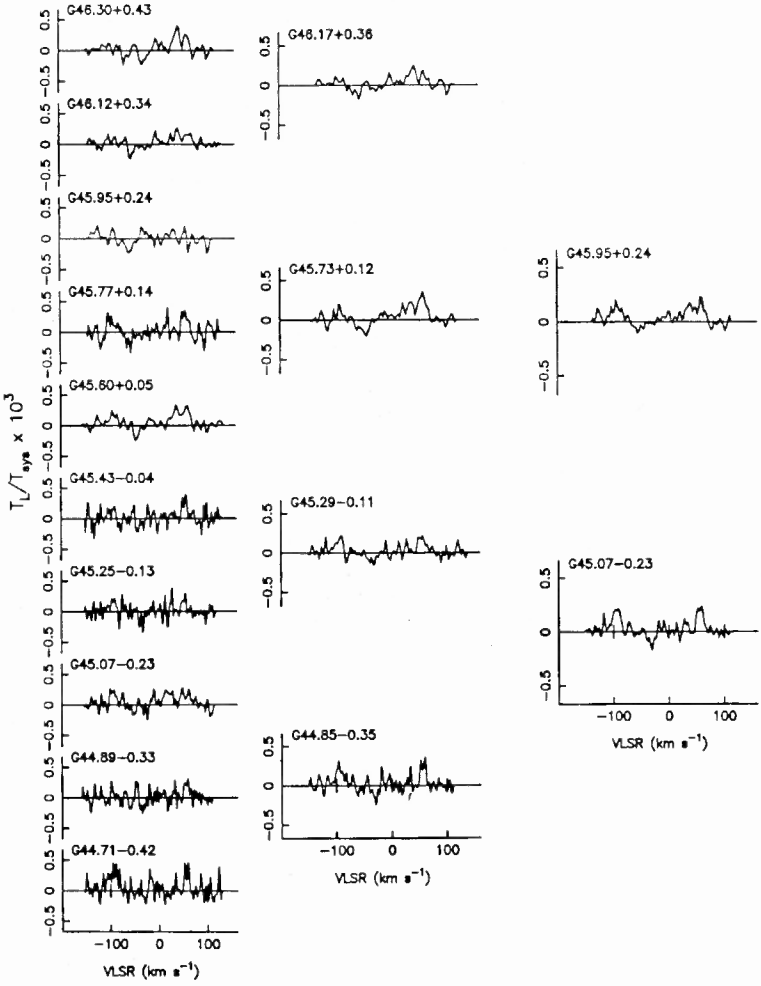

Figure 6.4: Spectra obtained by averaging different subsets of spectra observed towards field 7 (G45.5+0.0). The spectra shown in the left, center and right column are obtained by averaging over $2^\circ \times 12'$, $2^\circ \times 30'$ and $2^\circ \times 1^\circ$ area respectively. The galactic coordinates of the central of these angular region are shown on the spectra.

Table 6.4: Line parameters from the set of average spectra in field 7 (G45.5+0.0)

l (°)	b (°)	T_L/T_{sys} × 10^3	ΔV (km s^{-1})	$V_{\rm LSR}$ (km s^{-1})	V_{res} (km s^{-1})	RMS[1] × 10^3	t_{int} (hrs)	Note
Average over 2°× 12′								
46.30	+0.43	0.33(0.02)	33.0(1.1)	53.4(0.5)	8	0.09	21.1	
46.12	+0.34				8	0.09	19.3	
45.95	+0.24				8	0.10	20.5	
45.77	+0.14	0.34(0.03)	13.6(1.3)	57.6(0.6)	5	0.13	17.3	
45.60	+0.05	0.28(0.01)	39.8(2.5)	47.6(1.0)	8	0.08	24.8	
45.43	−0.04	0.33(0.03)	11.7(1.1)	55.0(0.5)	3	0.12	25.2	
45.25	−0.13	0.24(0.04)	10.1(2.1)	53.2(0.9)	3	0.11	22.3	t
45.07	−0.23	0.18(0.02)	26.4(3.8)	55.5(1.5)	5	0.09	24.3	t
		0.23(0.02)	19.4(2.6)	18.4(1.0)	5	0.09	24.3	t
44.89	−0.33	0.29(0.03)	11.6(1.2)	56.9(0.5)	3	0.11	19.5	t
44.71	−0.42	0.37(0.04)	10.4(1.4)	56.0(0.6)	3	0.12	18.5	
Average over 2°× 30′								
46.17	+0.36	0.15(0.02)	9.1(1.2)	62.9(0.5)	8	0.06	50.7	
		0.21(0.01)	15.8(1.2)	41.9(0.5)	8	0.06	50.7	
45.73	+0.12	0.30(0.02)	14.2(1.0)	59.0(0.4)	6	0.07	52.4	
		0.17(0.01)	29.3(3.2)	33.4(1.2)	6	0.07	52.4	
45.29	−0.11	0.20(0.02)	17.4(1.9)	54.9(0.8)	5	0.07	61.3	t
44.85	−0.35	0.30(0.03)	11.7(1.3)	56.0(0.5)	3	0.08	48.6	
Average over 2°× 1°								
45.95	+0.24	0.14(0.01)	35.2(2.6)	47.5(1.1)	6	0.05	103.1	
45.07	−0.23	0.24(0.02)	12.8(1.1)	55.3(0.5)	5	0.05	109.9	

1) RMS is in units of T_L/T_{sys}

Note: t – tentative detection

2.2. However the actual SNR of the line in the average spectrum is 5.9. This increased SNR clearly indicates that the line emission is not confined to only 3 positions but spread over the entire 2° region.

To determine the actual angular extent of line emission, the following analysis was made. Different subsets of the 20 spectra were averaged as shown in Fig. 6.4. The spectra in the left column are obtained by averaging the spectra at adjacent positions. Thus they are equivalent to observing with a beam of 2° × 12′. The spectra in the central column, obtained by averaging five adjacent spectra, have an effective beam of 2° × 0°.5. The rightmost column show spectra with an effective beam of 2° × 1°. Line parameters of all possible emission features in these spectra are derived and tabulated in Table 6.4. A narrow ($\sim$ 11 km s^{-1}) feature appears to be present in all the spectra in the longitude range G44.67−0.4 to G45.47−0.0 (Fig. 6.4). This feature does not seem to be present either in other individual spectra or in the spectrum averaged over 1° centered at G45.95+0.2 (see Fig. 6.4). Thus the region responsible for this line is less than 1° in extent. The central velocity of line emission indicate a kinematic distance to the line emitting region of 6.3 kpc and the estimated size of the region is $\sim$ 110 pc. The individual spectra towards the positions G46.35+0.4 to G45.56−0.0 of field 7 (see Table 6.1) do not seem to have a common component although the integrated spectrum obtained by averaging them to an effective beam of 2° × 1° shows a broad feature ($\sim$ 35 km s^{-1}). Such broad features are also present in the spectra obtained by averaging over a 2° × 12′ region centered on G46.30+0.43 and G45.6+0.05 (see Fig. 6.4). These regions contain known H II regions. The 2.7 GHz continuum emission from the H II region G46.495−0.247 overlaps with the 2° × 12′ region centered on G46.30+0.43 (see Fig. 6.16). The 2° × 12′ region centered on G45.60+0.05 contains the H II regions G45.475+0.13 and G45.451+0.06. The central velocities of the features seen in the integrated spectra towards G46.30+0.43 and G45.60+0.05 are comparable with those obtained from the H II regions. We conclude that the line emission towards field G45.5+0.0 constitute discrete emission zones and some of them have an angular size as large as a degree or more. There is some evidence for the line emission zones to be associated with the H II regions in the field.

6.7 Summary

In this chapter we have presented the RRL observations made using the full ORT (i.e. all 22 modules) which gives an angular resolution of 2° × 6′. These observations were used to understand the nature of clumpiness in line emission observed in the low resolution survey. Seven 2° wide fields and two 6° wide fields in the inner Galaxy were observed with the 2° × 6′ beam. A total of 252 spectra were obtained from the higher resolution observations. RRLs were detected in almost all individual positions within the fields with $l < 35°$ and at several individual positions within the fields in the longitude range $l = 35°$ to 85°. The line width observed in these observations were in the range 20 km s^{-1} to 40 km s^{-1} . The integrated spectrum obtained by averaging 20 spectra towards a 2° × 2° region in most cases is similar to the spectrum observed in the low resolution survey towards the same direction. Analysis of line emission in the high resolution observations towards fields with $l < 35°$ indicates that the line emitting region is extended over several degrees but is clumpy. The clump size can be $\sim$ 10 pc or less. Detailed analysis of the data towards field 7, G45.5+0.0, shows that the line emission consists of discrete zones of ionized region. The angular extent of these zones

are likely to be one degree or more corresponding to a linear sizes of > 110 pc at the kinematic distance obtained from the central velocity of line emission. There is some evidence for the line emitting zones being associated with the H II regions in this field.

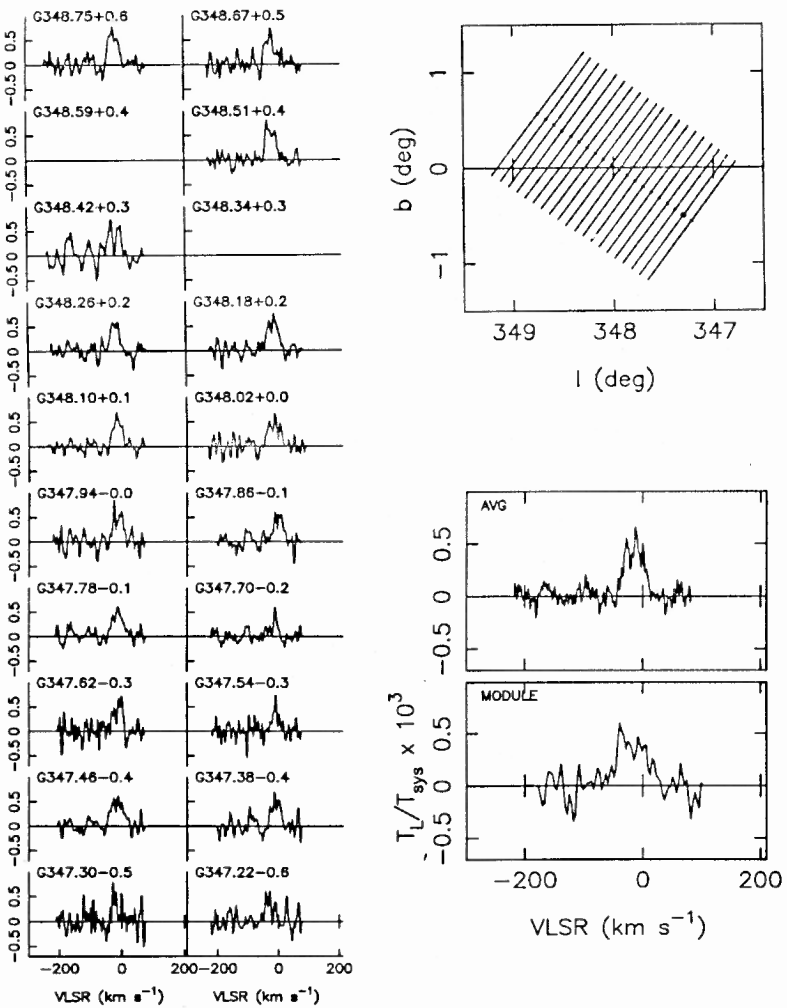

Figure 6.5: The spectra observed towards field 1 (G348.0+0.0) with a beam of 2° × 6′ are shown in the left. The feature seen "near" 0 km s^{-1} is the hydrogen line. The positions observed are shown in the top right corner where the dots indicate the beam center and the length of the line represent the extent of the 2° beam of the ORT. The spectrum (labeled as AVG) obtained by averaging all the 20 spectra and the spectrum (labeled as MODULE) obtained by a 2° × 2° beam in the same direction are shown in the bottom right corner. The ordinate of the spectra are in units of T_L/T_{sys} and abscissa are in LSR velocity with respect to the hydrogen line.

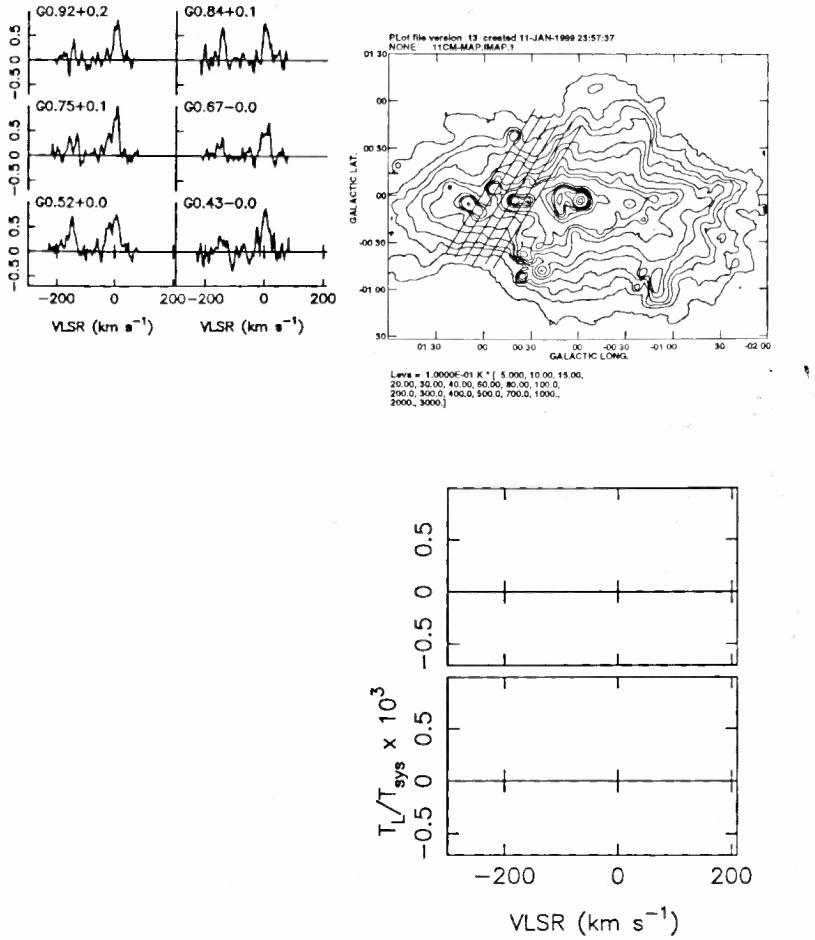

Figure 6.6: The spectra observed towards field 2a with a beam of 2° × 6′ are shown in the left. The feature seen "near" 0 km s^{-1} is the hydrogen line. The observed positions are marked on the 11 cm continuum map (Reich et al. 1990; top right corner). The average spectrum is not shown here since the observations towards this field do not sample a 2° × 2° region.The line passes through the center of the 2° × 6′ beam with its length representing the 2° extent. The ordinate of the spectra are in units of T_L/T_{sys} and abscissa are in LSR velocity with respect to the hydrogen line.

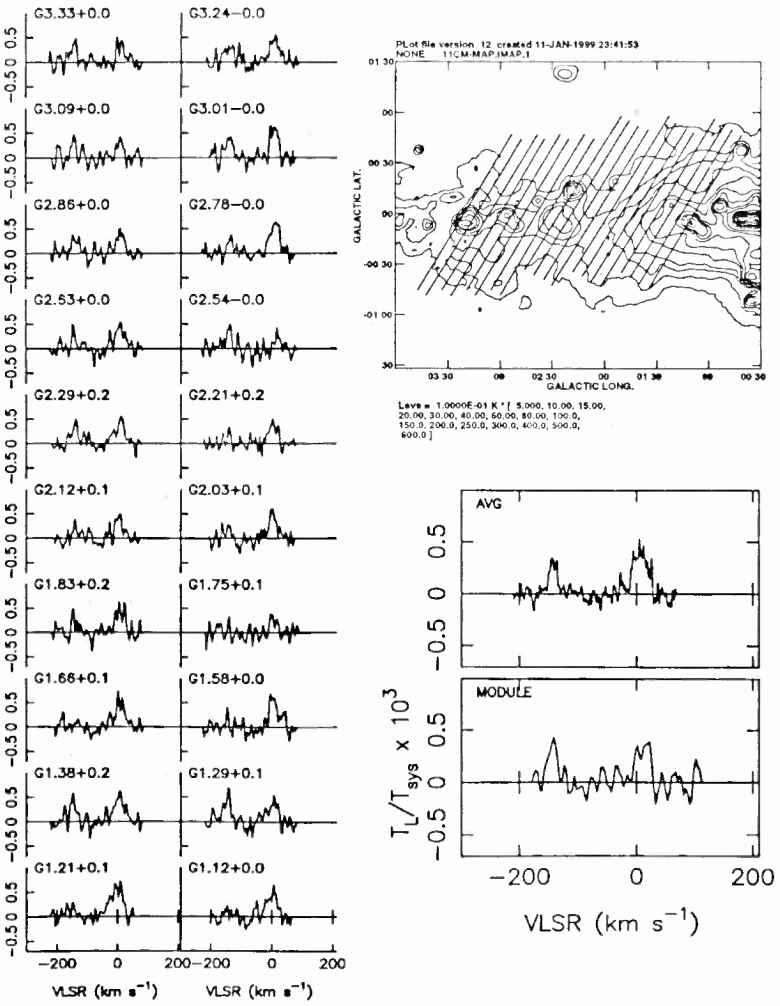

Figure 6.7: The spectra observed towards field 2b (G2.3+0.0) with a beam of 2° × 6′ are shown in the left. The feature seen "near" 0 km s^{-1} is the hydrogen line. The observed positions are marked on the 11 cm continuum map (Reich et al. 1990; top right corner). The line passes through the center of the 2° × 6′ beam with its length representing the 2° extent. The spectrum (labeled as AVG) obtained by averaging all the 20 spectra and the spectrum (labeled as MODULE) obtained by a 2° × 2° beam in the same direction are shown in the bottom right corner. The ordinate of the spectra are in units of T_L/T_{sys} and abscissa are in LSR velocity with respect to the hydrogen line.

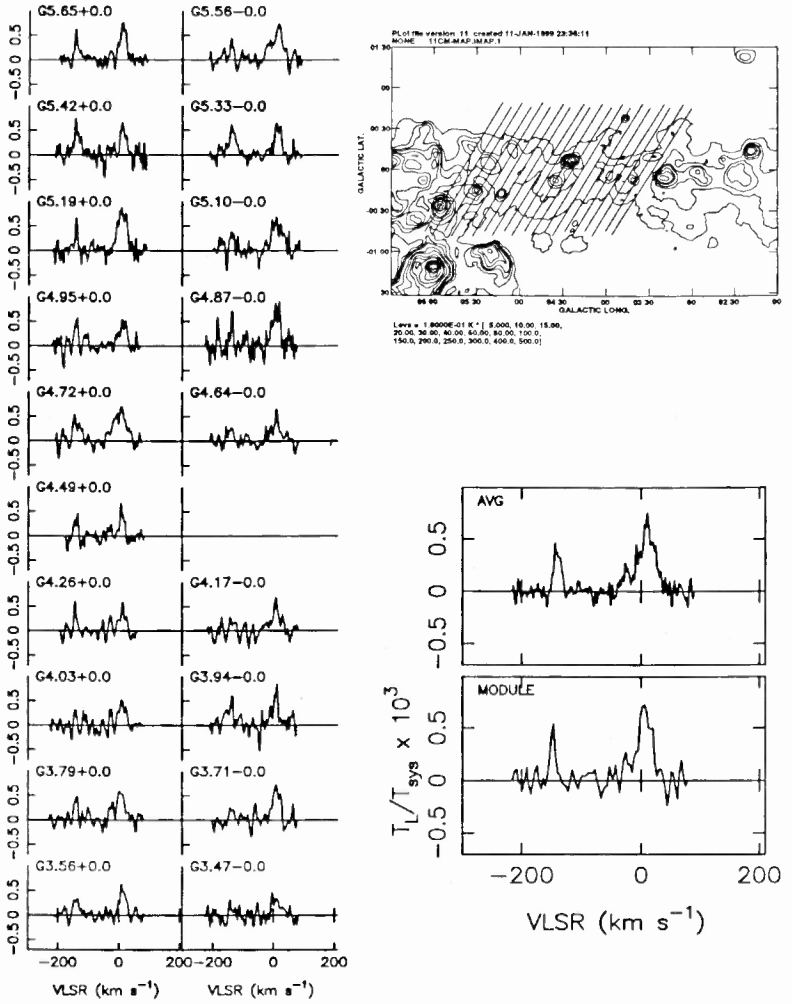

Figure 6.8: The spectra observed towards field 2c (G4.7+0.0) with a beam of 2° × 6′ are shown in the left. The feature seen "near" 0 km s^{-1} is the hydrogen line. The observed positions are marked on the 11 cm continuum map (Reich et al. 1990; top right corner). The line passes through the center of the 2° × 6′ beam with its length representing the 2° extent. The spectrum (labeled as AVG) obtained by averaging all the 20 spectra and the spectrum (labeled as MODULE) obtained by a 2° × 2° beam in the same direction are shown in the bottom right corner. The ordinate of the spectra are in units of T_L/T_{sys} and abscissa are in LSR velocity with respect to the hydrogen line.

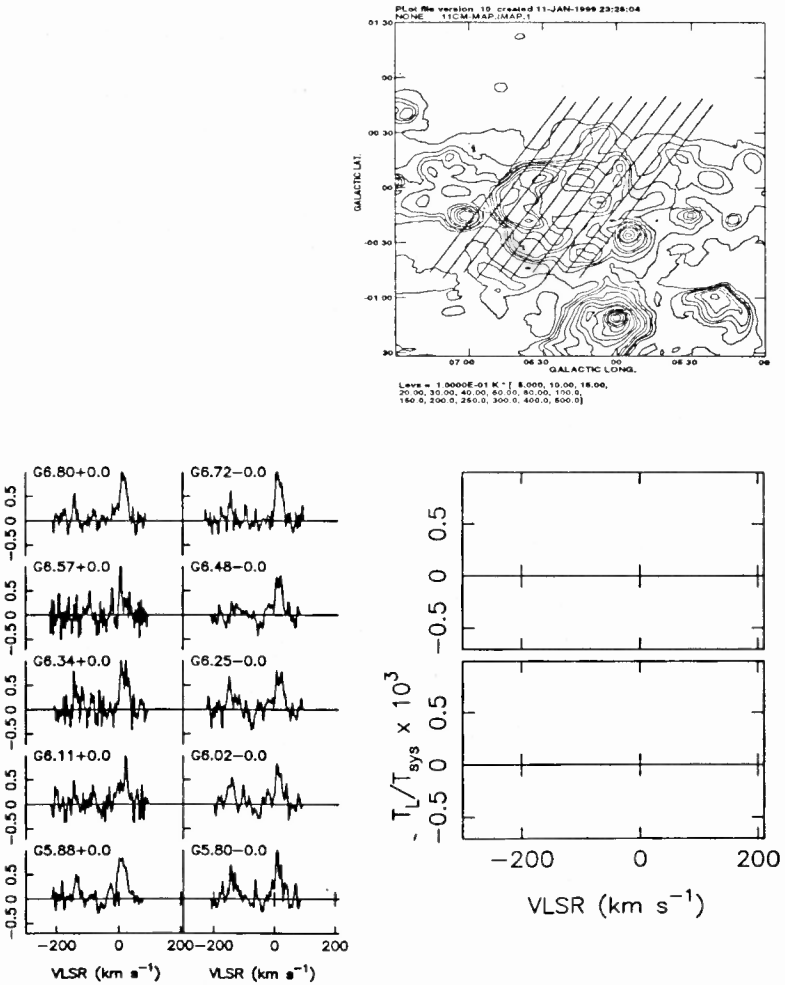

Figure 6.9: The spectra observed towards field 2d with a beam of 2° × 6′ are shown in the left. The feature seen "near" 0 km s^{-1} is the hydrogen line. The observed positions are marked on the 11 cm continuum map (Reich et al. 1990; top right corner). The average spectrum is not shown here since the observations towards this field do not sample a 2° × 2° region. The line passes through the center of the 2° × 6′ beam with its length representing the 2° extent. The ordinate of the spectra are in units of T_L/T_{sys} and abscissa are in LSR velocity with respect to the hydrogen line.

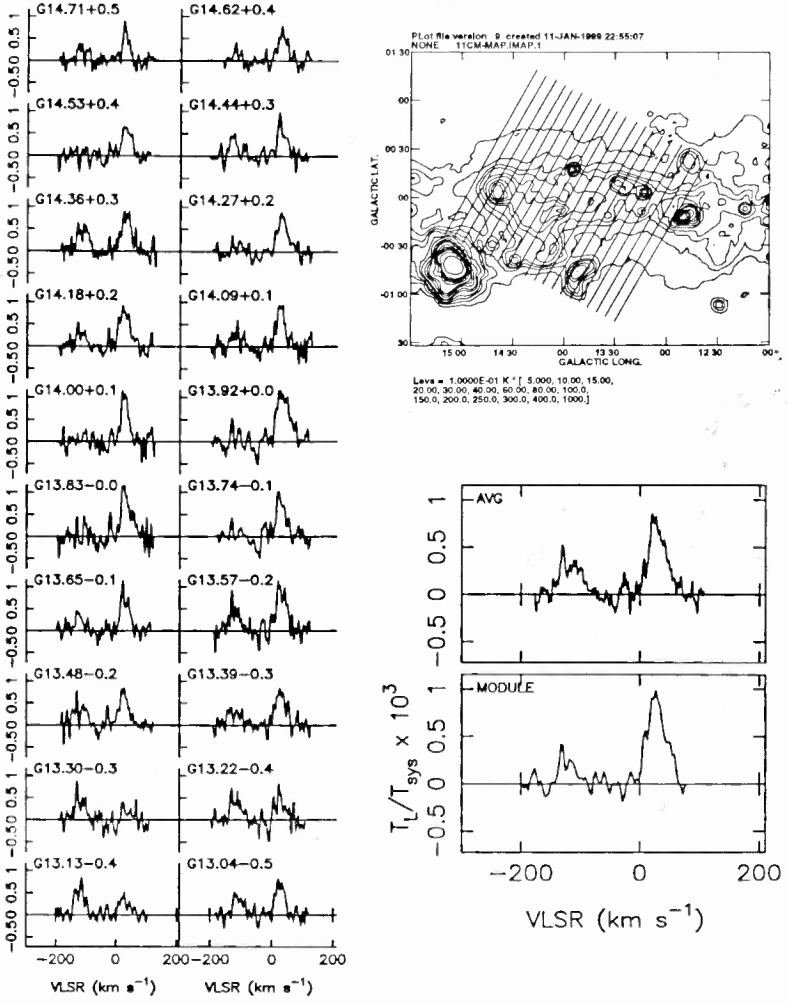

Figure 6.10: The spectra observed towards field 3 (G13.9+0.0) with a beam of 2° × 6′ are shown in the left. The feature seen "near" 25 km s^{-1} is the hydrogen line. The observed positions are marked on the 11 cm continuum map (Reich et al. 1990; top right corner). The line passes through the center of the 2° × 6′ beam with its length representing the 2° extent. The spectrum (labeled as AVG) obtained by averaging all the 20 spectra and the spectrum (labeled as MODULE) obtained by a 2° × 2° beam in the same direction are shown in the bottom right corner. The ordinate of the spectra are in units of T_L/T_{sys} and abscissa are in LSR velocity with respect to the hydrogen line.

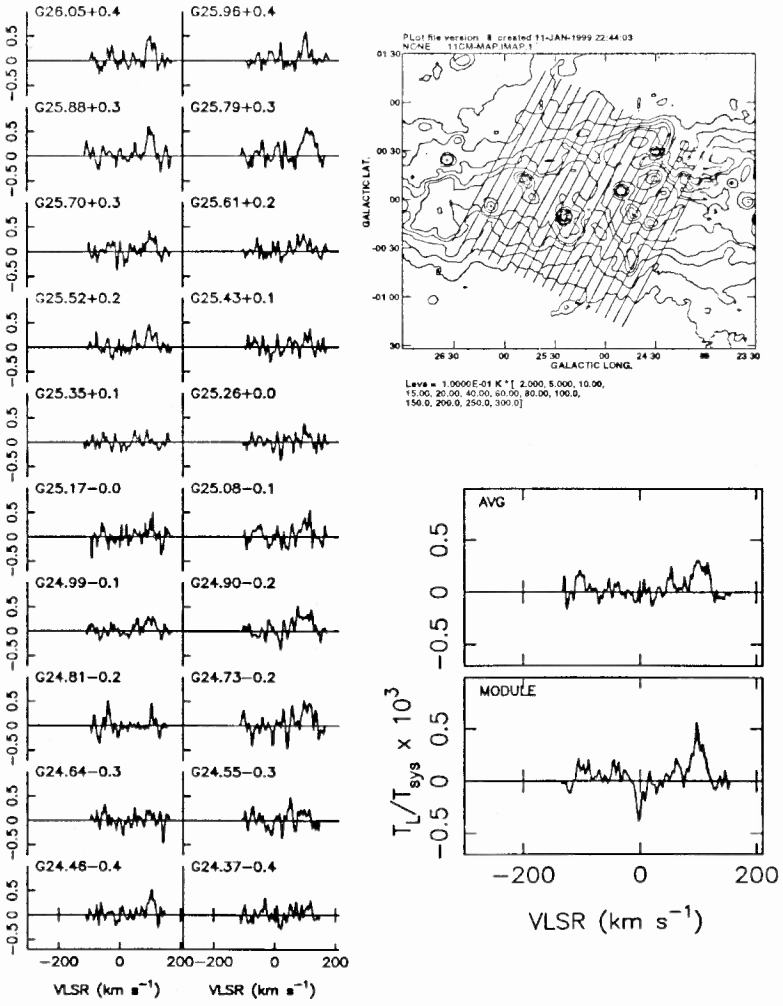

Figure 6.11: The spectra observed towards field 4 (G25.2+0.0) with a beam of 2° × 6′ are shown in the left. The feature seen "near" 100 km s^{-1} is the hydrogen line. The observed positions are marked on the 11 cm continuum map (Reich et al. 1990; top right corner). The line passes through the center of the 2° × 6′ beam with its length representing the 2° extent. The spectrum (labeled as AVG) obtained by averaging all the 20 spectra and the spectrum (labeled as MODULE) obtained by a 2° × 2° beam in the same direction are shown in the bottom right corner. The ordinate of the spectra are in units of T_L/T_{sys} and abscissa are in LSR velocity with respect to the hydrogen line.

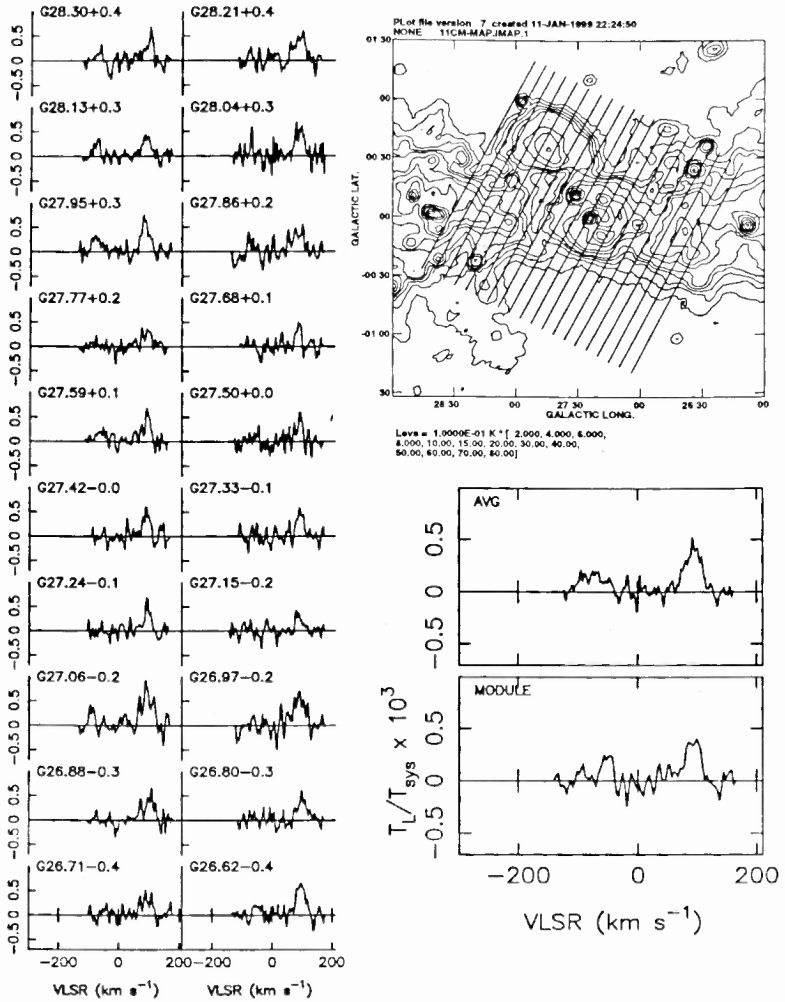

Figure 6.12: The spectra observed towards field 5 (G27.5+0.0) with a beam of 2° × 6′ are shown in the left. The feature seen "near" 90 km s^{-1} is the hydrogen line. The observed positions are marked on the 11 cm continuum map (Reich et al. 1990; top right corner). The line passes through the center of the 2° × 6′ beam with its length representing the 2° extent. The spectrum (labeled as AVG) obtained by averaging all the 20 spectra and the spectrum (labeled as MODULE) obtained by a 2° × 2° beam in the same direction are shown in the bottom right corner. The ordinate of the spectra are in units of T_L/T_{sys} and abscissa are in LSR velocity with respect to the hydrogen line.

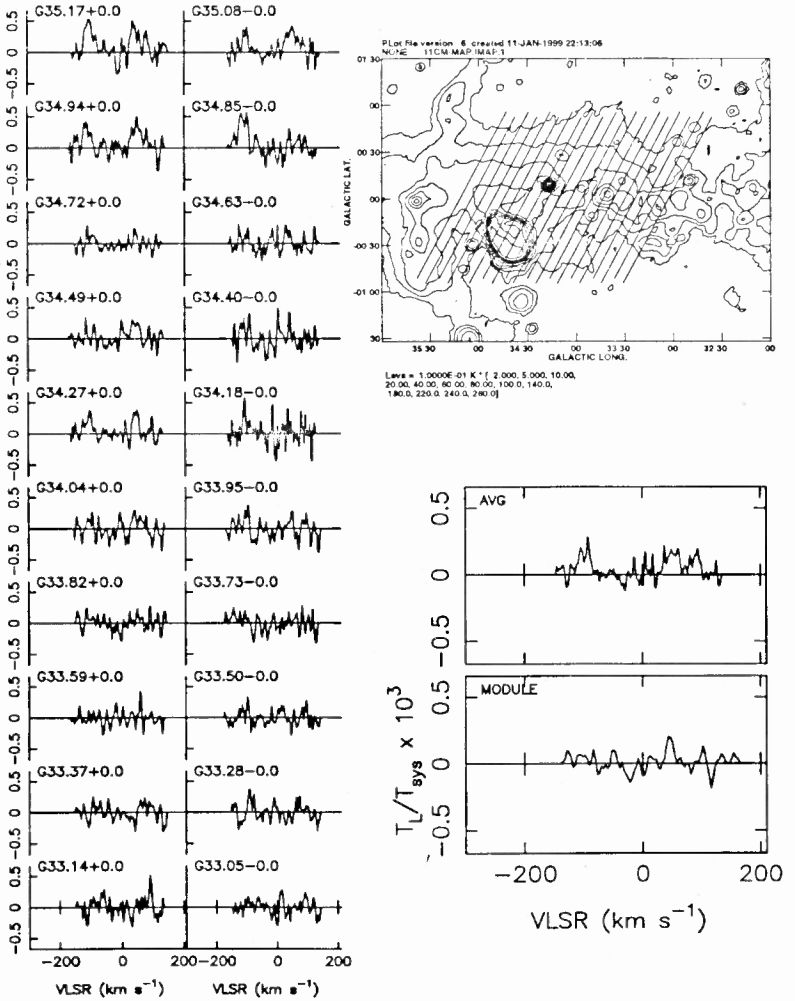

Figure 6.13: The spectra observed towards field 6a (G34.2+0.0) with a beam of 2° × 6′ are shown in the left. The feature seen "near" 50 km s^{-1} is the hydrogen line. The observed positions are marked on the 11 cm continuum map (Reich et al. 1990; top right corner). The line passes through the center of the 2° × 6′ beam with its length representing the 2° extent. The spectrum (labeled as AVG) obtained by averaging all the 20 spectra and the spectrum (labeled as MODULE) obtained by a 2° × 2° beam in the same direction are shown in the bottom right corner. The ordinate of the spectra are in units of T_L/T_{sys} and abscissa are in LSR velocity with respect to the hydrogen line.

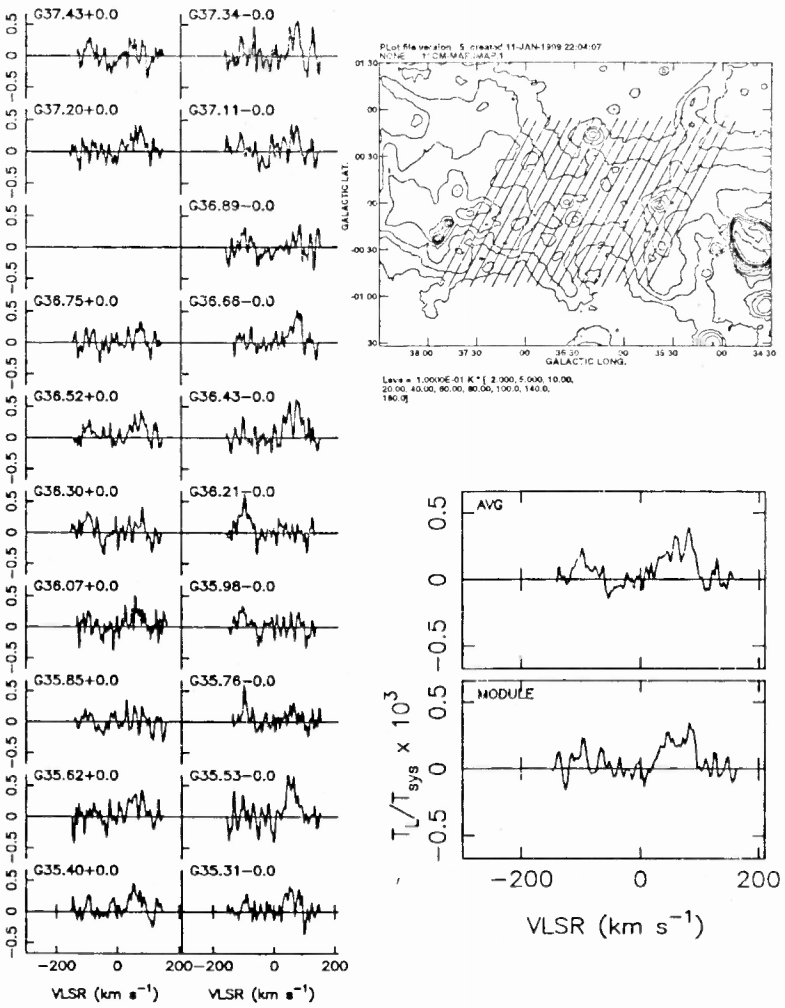

Figure 6.14: The spectra observed towards field 6b (G36.5+0.0) with a beam of 2° × 6′ are shown in the left. The feature seen "near" 70 km s^{-1} is the hydrogen line. The observed positions are marked on the 11 cm continuum map (Reich et al. 1990: top right corner). The line passes through the center of the 2° × 6′ beam with its length representing the 2° extent. The spectrum (labeled as AVG) obtained by averaging all the 20 spectra and the spectrum (labeled as MODULE) obtained by a 2° × 2° beam in the same direction are shown in the bottom right corner. The ordinate of the spectra are in units of T_L/T_{sys} and abscissa are in LSR velocity with respect to the hydrogen line.

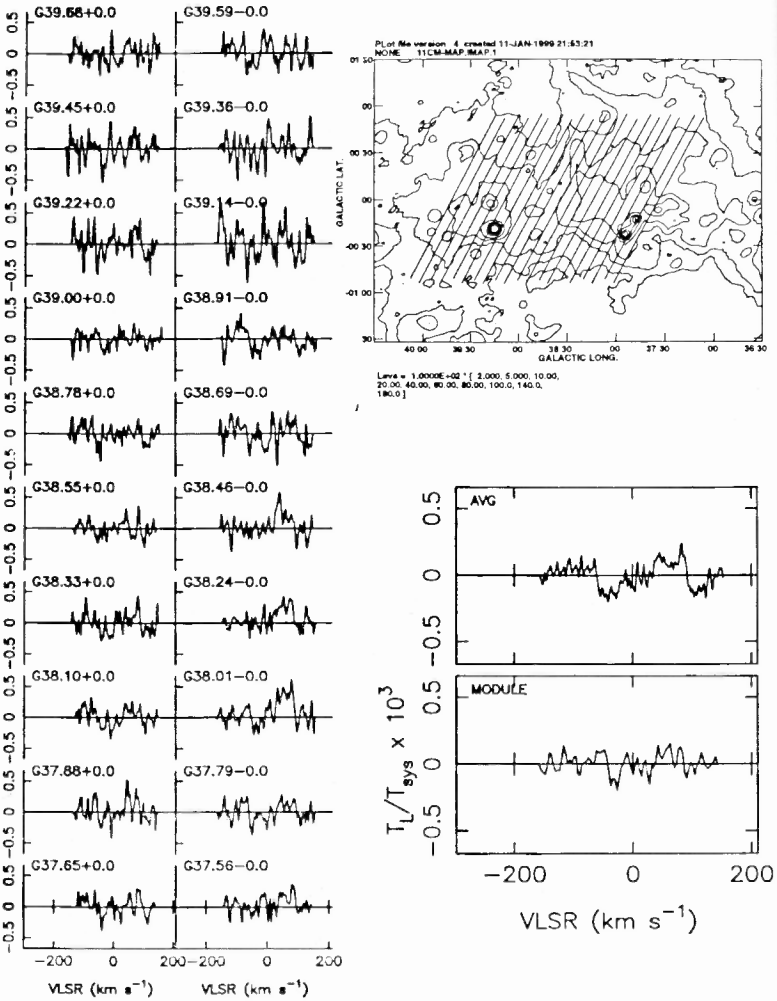

Figure 6.15: The spectra observed towards field 6c (G38.7+0.0) with a beam of 2° × 6′ are shown in the left. The feature seen "near" 60 km s^{-1} is the hydrogen line. The observed positions are marked on the 11 cm continuum map (Reich et al. 1990; top right corner). The line passes through the center of the 2° × 6′ beam with its length representing the 2° extent. The spectrum (labeled as AVG) obtained by averaging all the 20 spectra and the spectrum (labeled as MODULE) obtained by a 2° × 2° beam in the same direction are shown in the bottom right corner. The ordinate of the spectra are in units of T_L/T_{sys} and abscissa are in LSR velocity with respect to the hydrogen line.

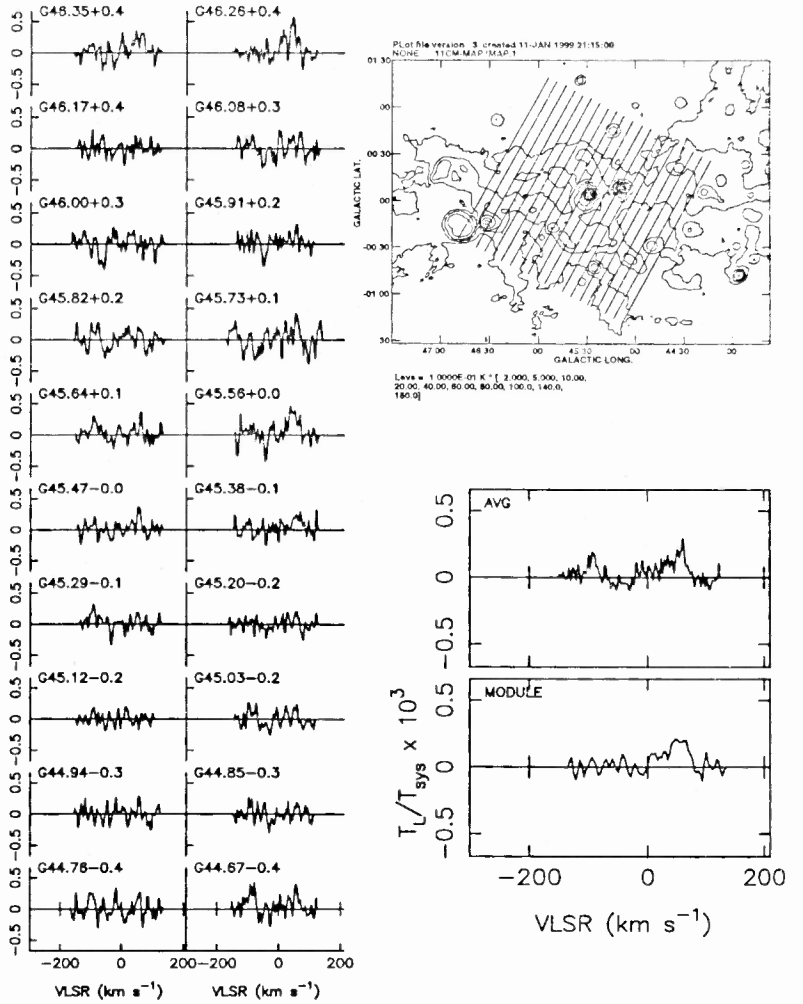

Figure 6.16: The spectra observed towards field 7 (G45.5+0.0) with a beam of 2° × 6′ are shown in the left. The feature seen "near" 45 km s^{-1} is the hydrogen line. The observed positions are marked on the 11 cm continuum map (Reich et al. 1990; top right corner). The line passes through the center of the 2° × 6′ beam with its length representing the 2° extent. The spectrum (labeled as AVG) obtained by averaging all the 20 spectra and the spectrum (labeled as MODULE) obtained by a 2° × 2° beam in the same direction are shown in the bottom right corner. The ordinate of the spectra are in units of T_L/T_{sys} and abscissa are in LSR velocity with respect to the hydrogen line.

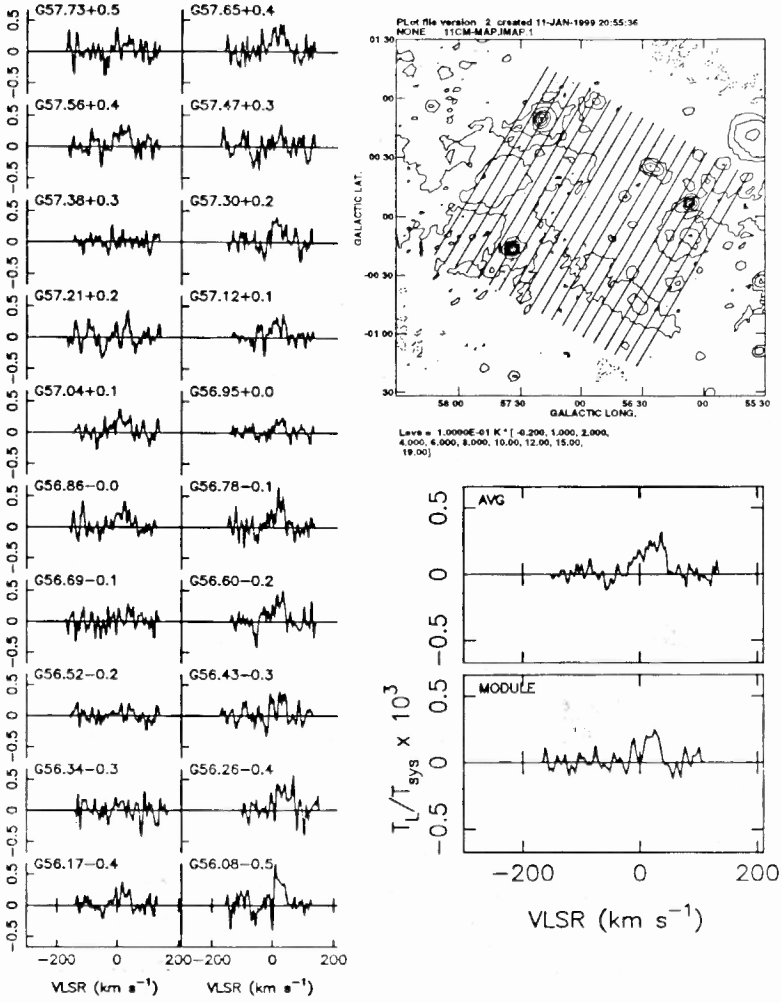

Figure 6.17: The spectra observed towards field 8 (G56.9+0.0) with a beam of 2° × 6′ are shown in the left. The feature seen "near" 25 km s^{-1} is the hydrogen line. The observed positions are marked on the 11 cm continuum map (Reich et al. 1990: top right corner). The line passes through the center of the 2° × 6′ beam with its length representing the 2° extent. The spectrum (labeled as AVG) obtained by averaging all the 20 spectra and the spectrum (labeled as MODULE) obtained by a 2° × 2° beam in the same direction are shown in the bottom right corner. The ordinate of the spectra are in units of T_L/T_{sys} and abscissa are in LSR velocity with respect to the hydrogen line.

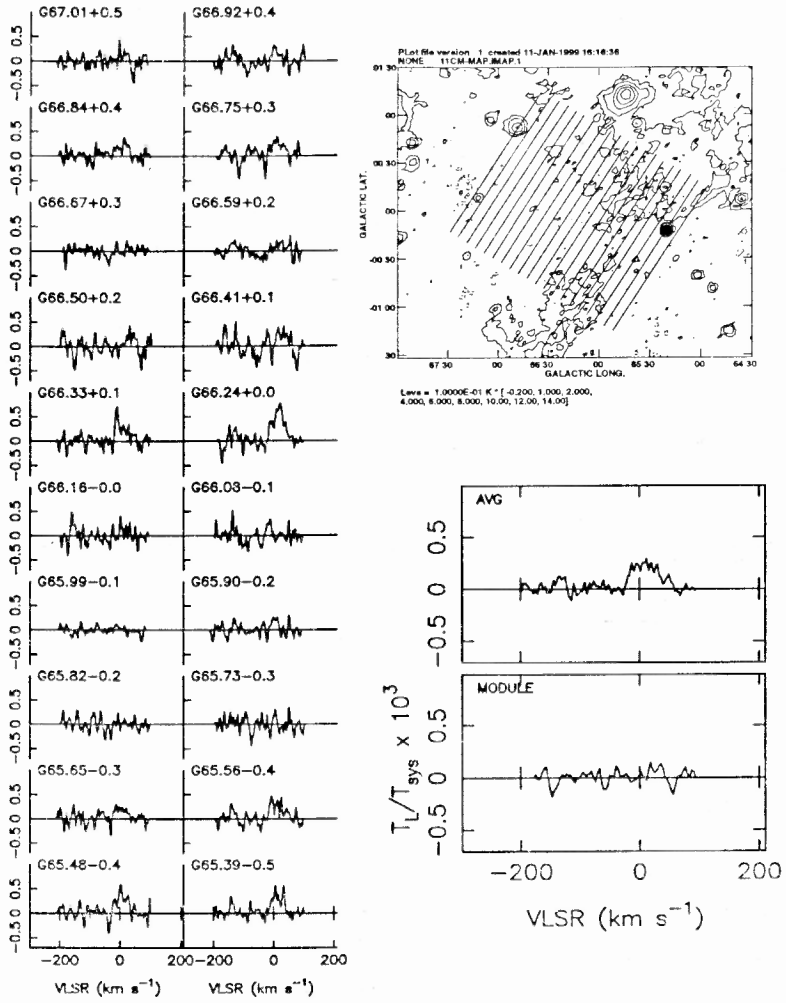

Figure 6.18: The spectra observed towards field 9 (G66.2+0.0) with a beam of 2° × 6′ are shown in the left. The feature seen "near" 0 km s^{-1} is the hydrogen line. The observed positions are marked on the 11 cm continuum map (Reich et al. 1990; top right corner). The line passes through the center of the 2° × 6′ beam with its length representing the 2° extent. The spectrum (labeled as AVG) obtained by averaging all the 20 spectra and the spectrum (labeled as MODULE) obtained by a 2° × 2° beam in the same direction are shown in the bottom right corner. The ordinate of the spectra are in units of T_L/T_{sys} and abscissa are in LSR velocity with respect to the hydrogen line.